A slender compliant mechanism for back support with non-linear behavior

Master Thesis

Saralina Koentges

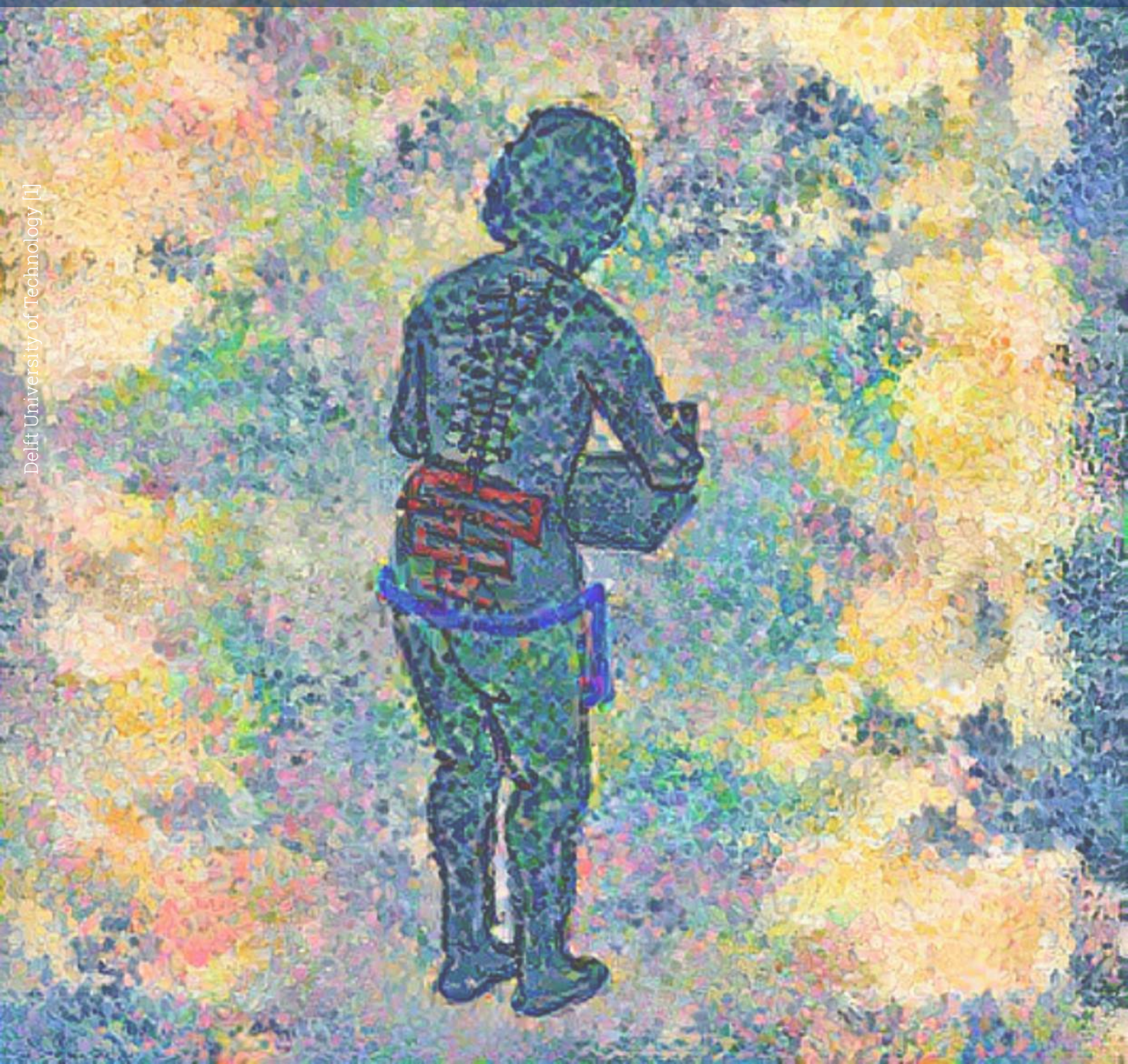

Delft University of Technology

A slender compliant mechanism for back support with non-linear behavior

by

Saralina Koentges

to obtain the degree of Master of Science
at the Delft University of Technology,
to be defended publicly on July 31, 2023 at 14:30.

Student number:	5633982	
Project duration:	November 1, 2022 – July 31, 2023	
Thesis committee:	Prof. dr. ir. J.L. Herder,	TU Delft, chair
	Ir. A. Amoozandeh Nobaveh,	TU Delft, daily supervisor
	Ir. S.J. Wagemaker,	Laevo B.V., daily supervisor
	Dr. ir. R.A.J. van Ostayen	TU Delft, external member

This thesis is confidential and cannot be made public until July 31, 2024.

TU Delft

laevo
exoskeletons

Preface

Five years ago, my journey in mechanical engineering began in Brussels at the Vrije Universiteit Brussel (VUB), with uncertainty about where it would ultimately lead. During this time, I had the privilege of meeting individuals who awakened my curiosity for prosthetics, orthosis, and exoskeletons. These encounters became the driving force behind my decision to pursue further studies in mechanical engineering at the TU Delft, with a specific focus on the intersection of engineering and medicine.

Throughout my master's program, I had the opportunity to engage in various projects, including an enriching internship on hand prosthetics at Moveable. Additionally, I embarked on a significant milestone by undertaking a master's thesis at Laevo, an exoskeleton company. Although representing a fraction of my comprehensive studies, this thesis marks the completion of this academic cycle.

I am deeply grateful to the individuals who have supported me along this journey, as their assistance has been instrumental in making this thesis a reality. Firstly, I would like to express my sincere gratitude to Mike and Bas from Laevo. Thank you for the invaluable brainstorming sessions, your assistance in prototyping, experimental testing, proofreading, and the constant emotional support you provided. I also deeply appreciate the entire Laevo team for creating a memorable experience and warmly welcoming me into your team.

Of course, the successful completion of a master's thesis would not have been possible without the guidance of a supervisor. I am thankful to Ali for his time and guidance throughout the process. His support played an important role in my understanding of the project's scope and provided meaningful insights that shaped its direction. Regular meetings and Ali's initial supervision established a solid foundation for a successful outcome.

I would also like to extend my gratitude to Giuseppe, who stepped into the supervisory role for the final five weeks with dedication. His commitment ensured a seamless process and guided me through the critical final milestone of my thesis project.

Additionally, I would like to express my appreciation to Frank from Intespring for his openness and willingness to allow me to use the sensor, which helped save time for my project. Your support played a crucial role in the success of this master thesis.

Last but not least, I want to express my heartfelt gratitude for my parents', family's and friends' continuous support during my studies. Your presence in my life has been a constant source of inspiration and encouragement, and I am truly grateful for your involvement in this important project.

Saralina Koentges
Delft, July 2023

Contents

1

Introduction

Workers involved in physical labor, such as those in healthcare, agriculture, and airport luggage handling, frequently perform repetitive bending movements that strain their backs. These activities are often carried out for several hours each day, and can lead to back overloading when the muscles do not have sufficient time to recover or when the weight being lifted is excessive. This strain occurs as the back muscles contract, pulling the vertebrae closer together. Figure 1.1 illustrates a person's spine with the key back muscles (spinalis, longissimus, and iliocostalis) responsible for maintaining a straight posture [2]. The crossed dot represents the center of mass of the upper body, which lies in front of the vertebrae, necessitating muscle contraction to keep the back straight and upright. When carrying objects, the center of mass displaces further away from the vertebrae, which demands even greater muscle contraction. Consequently, lifting heavy objects can result in back pain, requiring muscle rest. However, in previously mentioned cases, individuals must use these muscles daily without adequate rest, leading to excessive muscle contraction that compresses the vertebrae, causing long-term degradation and discomfort.

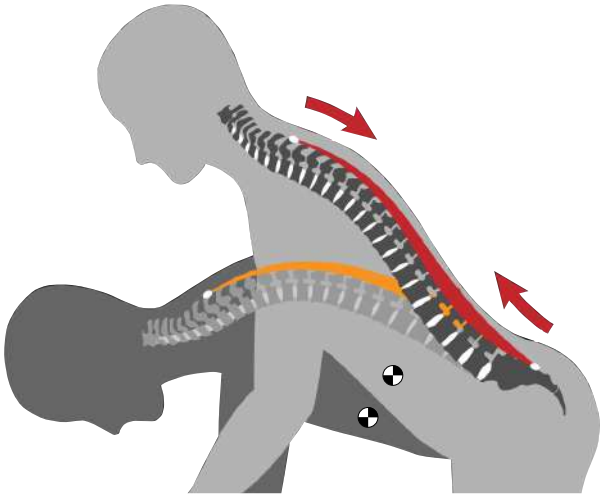

Figure 1.1: Side view of spine and muscles, the dots represent the center of mass of upper body [2].

Exoskeletons offer a potential solution, and there are two types: passive and active exoskeletons. The latter uses actuators or motors for movement, while passive exoskeletons do not require external energy sources. Instead, they store and release energy using specific materials, springs, or dampers [4]. One example of a passive exoskeleton is the Laevo FLEX developed by Laevo, which supports the lower back by using gas springs to store energy during bending [3]. When returning to an upright position, these gas springs revert to their original state, releasing the stored energy to the wearer. Figure 1.2a presents an image of the Laevo FLEX exoskeleton. The degree of support provided by the exoskeleton depends on the angle between the upper body and the individual's upper legs, as

shown in the moment-angle graph Figure 1.2b. As bending occurs, the support level varies accordingly. This moment-angle behavior is achieved by compressing the gas spring using a cam with a specific profile, resulting in a non-linear moment-angle characteristic. Different spring strengths are employed to accommodate the varying support requirements of individuals based on their height and weight. The behavior of the FLEX exoskeleton is demonstrated in Figure 1.2b, where the support is initially high during forward bending. However, as the angle between the back and upper legs reaches 20° to 40°, the support gradually decreases to facilitate continued bending without increasing difficulty. If the moment-angle relationship were linear, excessive support would prevent individuals from reaching their feet. Moreover, when the wearer bends, the passive tissue, including tendons, undergoes stretching, leading to decreased support demands as the tendons contribute to the overall support.

The combination of the gas spring and cam profile is referred to as a smart joint, existing out of multiple parts and contributing significantly to the overall weight of the exoskeleton. Each exoskeleton requires two smart joints, weighing approximately 0.6kg each. Together with two deflectable beams, a hipframe, a vest, and legpads, the exoskeleton's weight totals around 4kg, with the smart joints accounting for 30% of the overall weight.

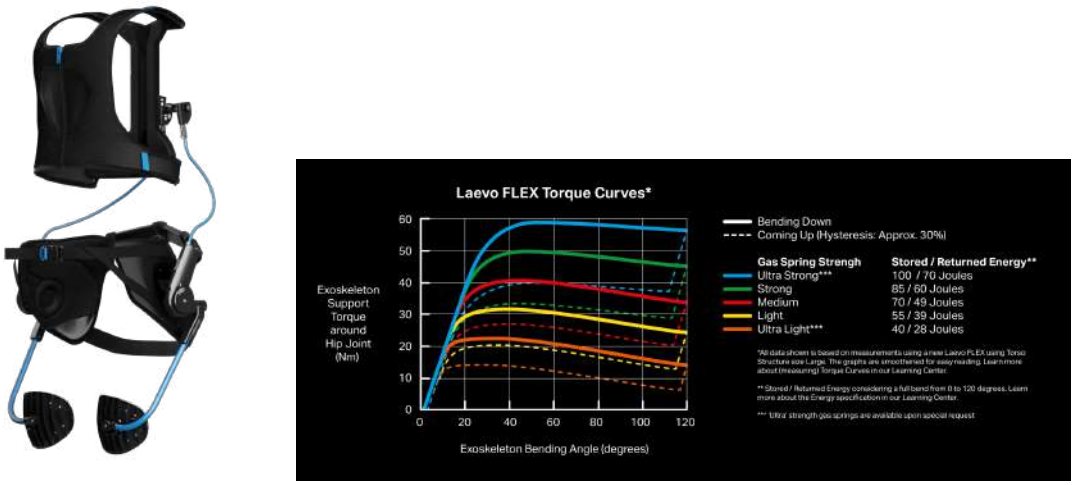

(a) Laevo FLEX design **(b)** Moment-angle curve

Figure 1.2: Laevo FLEX [3]

One potential solution to address the weight issue, particularly the number of components involved, is replacing the smart joints with a Compliant Mechanism (CM). CMs employ the elastic deformation of flexible parts instead of hinges, such as in conventional mechanisms, which often suffer from weight, complexity, and wear-related problems. CMs generally have fewer parts, are lighter, and exhibit reduced wear-related issues. However, CMs also have drawbacks, such as a limited range of motion, predominantly non-linear behavior, susceptibility to fatigue, and design challenges [6]. In the case of the Laevo FLEX, non-linear behavior is desirable, specifically a softening behavior characterized by decreasing stiffness with increasing deformation. This softening effect can be achieved using the contact-release principle, where several pre-tensioned springs are arranged in series and activated one at a time.

This thesis aims to develop a compliant spine prototype that exhibits a softening behavior similar to that of the Laevo FLEX, while also requiring fewer parts and a lighter construction. The contact release principle will be employed to achieve this softening behavior.

Chapter 2 will provide a comprehensive review of implementing non-linear stiffness for CMs, focusing on any non-linear stiffness, although the introduction of this thesis only mentions softening behavior. Chapter 3 will present a research paper exploring the use of contact-release of torsional beams in an open chain configuration to achieve a softening behavior. Chapter 4 will interpret the concept discussed in the research paper as a potential solution for exoskeletons. Finally, chapter 5 will present the conclusion. Appendices containing additional material not covered in the research paper will follow.

2

Literature Study

Review on Methods of Implementing Non-Linear Stiffness for Compliant Mechanisms

S.S.L. Koentges
Faculty of Mechanical, Maritime and Materials Engineering
Delft University of Technology
Delft, Zuid-Holland

***Abstract*—Compliant mechanisms with non-linear stiffness can be useful in multiple disciplines, such as aerospace engineering, medical devices, and soft robotics. In these fields, it is sometimes desired that a specific object has multiple purposes and a non-linear stiffness can be convenient. This work aims to provide an extensive overview of the existing solutions with different force-deflection characteristics, where the motion of the mechanism and corresponding stiffness characteristics are coupled. A main classification is made in function of the ways of changing the stiffness. This includes the change of boundary conditions, change in shape, and change in material properties. The next classification branches are based on the design of the concepts. The branches are split into state-based designs, jamming, contact-aided compliant mechanisms, cam-based designs for the change in boundary conditions, and in planar and spatial compliant mechanisms for shape changing. Additionally, the concepts are evaluated in function of their range of motion, strength, weight/size, size-strength-efficiency, number of parts, and type and direction of stiffness. The outcome of the classification, analyses, and evaluations of 31 different concepts will highlight the advantages and disadvantages of the mechanisms reviewed. The solutions based on jamming make up the largest group and includes the most complex concepts. In cam-based solutions the largest moments and forces are achieved. Applications with the largest range of motion can be found in the category of shape-changing. Further work should be done on creating concepts with a high size-strength efficiency and a large range of motion.**

***Index Terms*—Compliant Mechanisms, Non-Linear Stiffness, Jamming, Contact-Aided Compliant Mechanisms**

I. Introduction

Compliant Mechanisms (CM) are systems that use the elastic deformation of flexible parts to move instead of the conventional mechanisms. Most conventional mechanisms have problems of wear and backlash, which CM do not suffer from. Further advantages are that they are composed of fewer parts than rigid body mechanisms equivalents, and they are designed to be used in high-precision instrumentation. However, they have disadvantages such as a limited range of motion, mostly non-linear behavior, proneness to fatigue, and difficulty to design [1]. The disadvantage of having a non-linear behavior may also be beneficial, as it has been researched to have positive applications in certain fields, such as aerospace engineering, medical devices and soft robotics.

In the aerospace sector, morphing wings are of importance, as they improve flight performances, reducing fuel consumption. Non-linear stiffness is thus needed to achieve optimal wing shapes [2].

For minimally invasive surgery, the accessories must have a high stiffness to cut and grasp tissue, whilst having a low stiffness for moving within the body to prevent injuries to the surrounding human tissue [3]. The same applies for soft robotics and various actuators, high stiffness is needed when applying a high load and low stiffness is needed when applying a low load [4].

Extensive research has been conducted on non-linear or controllable stiffness of CM, where it is possible to change the stiffness at a chosen time, and the motion and stiffness are decoupled. Few, however give an overview of the existing solutions. One particular, a literature study of Staats' master thesis, gives an overview of variable stiffness mechanisms categorized by their working principle and includes a comparison and performance overview [5].

Tummala et al. [6] performed an overview of Contact-Aided Compliant Mechanisms (CACM) for applications in the aerospace field. Other papers primarily discuss design optimizations of CM with non-linear stiffness or how to non-linearly analyze and model them with certain software programs, such as Bruns and Tortorelli who discussed topology optimization of compliant mechanisms [7].

Three gaps in the existing state-of-the-art are present. Firstly, the reviews do not specifically discuss non-linear CM where the stiffness of the system is linked to its motion. This means that when a structure is elastically deformed, its stiffness changes throughout the motion. In some cases, the stiffness becomes higher when the force that causes the deformation increases. However, different scenarios are possible for the stiffness-motion coupling as the relationship is dependent on the force-deflection characteristic of the mechanism. The second gap entails the lack of experimental testing for the majority of analyzed solutions in existing reviews. The third gap is that the performance comparison of other papers miss the number of parts branch and the size-strength efficiency. This review aims (i) to have an overview of compliant structures that have a non-linear stiffness coupled to their motion where a prototype has been created to confirm the working principle, and (ii) to present a performance overview to compare the various concepts.

Section II details the selection and categorization process for the papers in this review. In Section III the working principle of the chosen concepts are explained. This is followed by Section IV where the different concepts are compared based on

their range of motion, strength, size and weight, size-strength efficiency, complexity, and type and direction of stiffness. Finally, in Section V a discussion about the proposed concepts and method is found.

II. Method

The search for relevant papers was performed on Google Scholar and Scopus. The selection method used search queries for word combinations such as ”compliant mechanism”, ”compliant spine”, ”compliant structure”, ”compliant beams” with ”non-linear stiffness”, ”softening”, ”stiffening”, and ”predefined force-displacement path”. After several initial categorizations, supplementary specific searches were executed e.g. CACM with non-linear stiffness. Additionally, the snowball method was used to find new relevant papers.

For the selection of the concepts of the chosen papers, the first criterion is related to the non-linear stiffness. If a concept has this characteristic, then all force-deflection paths as shown in Fig. 2 are possible. The second important criterion requires the discussed solutions or concepts to be experimentally validated by a functional prototype.

A tree diagram was made for the categorization, starting with the different methods to change the stiffness. There are three ways of achieving this, that is the change in boundary conditions, the shape, and the material properties. One could argue a fourth type; the change of pre-stress, but this is consequently changed when the boundary conditions are altered. Subsequent categorization is performed based on which aspect of the design of the concept made the mechanism non-linear. The branches of boundary conditions are state-based designs, jamming, CACM, and cam-based designs. Spatial and planar mechanisms are two possibilities considered to change shapes. For mechanical properties changes, no further classification is made, as this paper considers only one option. Further categorization is made if a second or perhaps a third design choice makes a difference between multiple concepts. The tree diagram can be seen in Fig. 1.

The existing force-deflection characteristics can be found in Fig. 2. In the reviewed concepts, the mechanisms only deform elastically and do not deform plastically. When applying a force, the CM deforms elastically. If by increasing the force on the mechanism, the mechanism is more resistant to deformation, it has a stiffening effect. On the force-deflection graph, this results in a J-curve. If, on the contrary, the mechanism is easier to deform by increasing the force, it has a softening effect.

A special case in the softening effect is the constant force path. This occurs when the mechanism first linearly deforms with increasing force until a certain force threshold is passed, then the mechanism can deform further without an increase in external force.

An even more extreme case is the occurrence of negative stiffness. Under a specifically applied load, the mechanism loses its stability and goes to another stable configuration requiring a lower external load. In the force-displacement path,

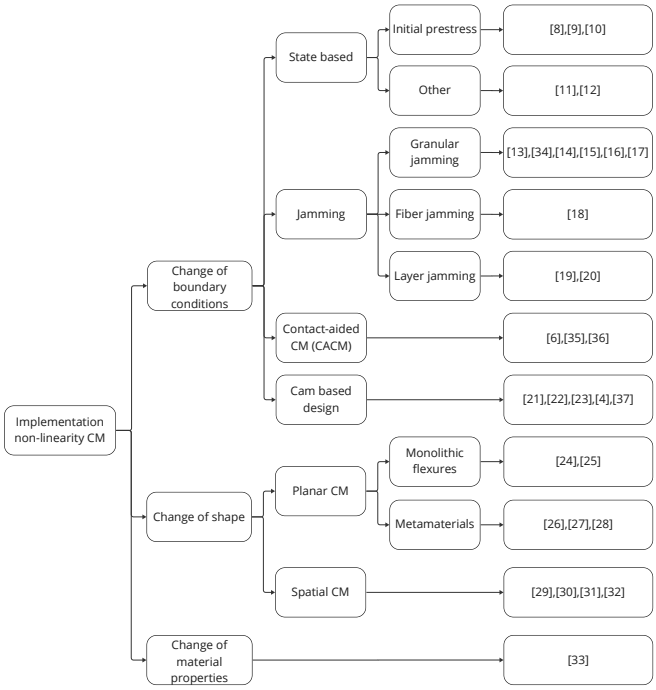

Fig. 1. Categorization tree

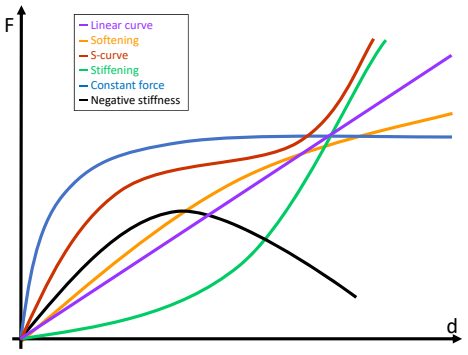

Fig. 2. Different non-linearities in the force-deflection path

the negative stiffness is the negative slope and the switch of stable configuration is called the snap-through phenomenon.

Another option entails an initial softening followed by a stiffening effect, thus creating an S-curve. This can result in three different softening-stiffening transitions depending on the effectiveness of the softening. The first possibility is that the softening effect is significant and achieves negative stiffness. Next, a constant force path takes place instead of the negative stiffness. A softening effect that has a small positive slope is the last possibility.

Fig. 3. Prototype of statically balanced inverted pendulum with three torsion bars [8]

III. Results

In the following section, all concepts corresponding to the criteria outlined in Section II and categorized in the tree diagram in Fig. 1 will be analyzed in greater detail.

A. Change of boundary conditions

By changing the boundary conditions, the stiffness behavior of certain concepts varies. Several examples of this behavior will be provided in the following paragraphs.

State-based designs

State-based designs are mechanisms where the physical structure varies. The change can be achieved in multiple ways, so two categories are created within this branch. The first category of the initial pre-stress of linear springs and the second category includes examples without initial pre-stress.

1) Initial pre-stress
   By stretching a linear spring in a non-linear way, a non-linear stiffness is achieved. The change in stretch of the spring is seen as a change in pre-stress of the spring.
   - In [8] an inverted pendulum is statically balanced by using three parallel torsion bars and mechanical stops, see Fig. 3. The torsional bars are pre-stressed, which is essential as this results in the system having a softening effect. The mechanical stops are used to block the effect of a certain torsional bar and allow the torsion bars to have a specific range of motion. As the torsion bars are positioned parallel, the stiffness is the sum of all three bars, when used at the same time. The range of motion is 90°. It is possible to adapt this setting. The paper however focused solely on the 90° rotation. Within this range of motion, there are three stable and three unstable positions. The advantage of torsion springs is that they do not require as much free space as linear springs. The maximum moment is 25 Nm and a balancing error of 0.35 Nm is found.
   - In [9] a bidirectional variable stiffness actuator (VSA) is created. Here non-linear stiffness comes from varying the pre-stress of a linear spring. The VSA exists of two fixed pulleys, one movable pulley, a string, and a linear spring attached to the movable pulley, see Fig.4. The two fixed pulleys are at the same height and the movable pulley is at an offset between the two fixed pulleys. The string touches all three pulleys. When the string tension is increased, the movable pulley compresses the linear spring. Thus, the linear spring has a different stress and non-linear stiffness is achieved.

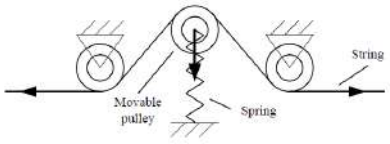

Fig. 4. VSA schematic [9]

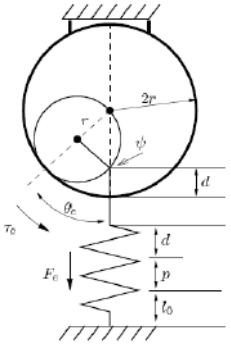

Fig. 5. A non-linear SEA [10]

   - In [10] a novel series elastic actuator (SEA) is proposed for a hopping robot. Here a linear spring is stretched in a nonlinear manner. The SEA exists of two circles: one small circle and another bigger one with twice the radius. The small circle is positioned inside the larger one. The linear spring is attached to the small circle. The inner circle rotates inside the outer circle without slipping. While rotating it stretches the spring. The spring is stretched in a straight line, see Fig. 5. To achieve high energy storage, the spring is able to deform significantly. Depending on the systems' pre-stress this concept can achieve moments from 30 Nm up to 50 Nm.

2) Other
   - In [11] a concept is proposed where the bending and torsional stiffness can be adjusted. The design includes a clamped-free beam with a 3D shape following 3 edges of a cube and a shorter bellow that can slide on the beam, see Fig. 6. The beam has high bending stiffness and low torsional stiffness. The bellow has high torsional stiffness and low bending stiffness. The bellow is 60 times stiffer in torsion compared to the beam and the beam is 10 times stiffer in bending compared to the bellow. By sliding the bellow over the beam, the endpoint displacement changes,

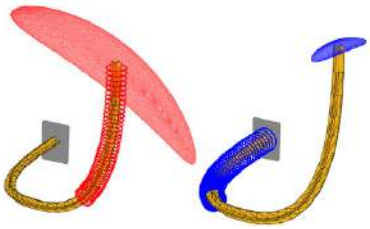

Fig. 6. Endpoint displacement of concept dependent on the placement of torsional stiffener on beam [11]

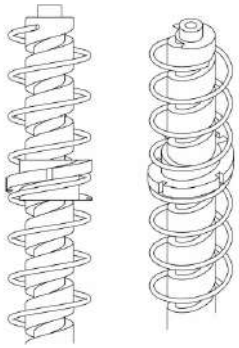

Fig. 7. Spindle and nut inside spring that constrain the number of used springs for a gravity balancer [12]

thus changing the stiffness. The stiffness does not only depend on the bellows' placement but also on its length. The stiffness is not equivalent in all directions.

- In [12] a spring and a spindle are used to create non-linear stiffness in a gravity balancer. Here the non-linearity comes from varying the number of coils on the spring. This is done by placing a spindle with a rotating nut inside a spring. The spindle, nut, and spring all have the same pitch, so when the nut rotates around the spindle, the spring stays in place. By displacing the nut, the number of active coils varies, and thus the stiffness can be adjusted.

Jamming

Jamming is another way to change the stiffness of a mechanism. There are three types of jamming: granular, fiber, and layer jamming [13]. The stiffness varies based on the way particles/ fibers or layers are packed. If the particles/ fibers or layers are more densely packed, friction increases, and motion is more constrained resulting in higher stiffness. To adjust the density, a change in pressure is used. This can be achieved by an external pump or tendon [14]. The packing of the particles can be attained by increasing the external pressure. This pushes the particles against each other and is called positive pressure jamming. The other pressure-related option is to decrease the pressure at the place where the particles are. This is called negative pressure jamming. The particles are pressed against each other because the volume is decreasing. It should be noted that at the same pressure, the non-linear behavior is a softening behavior. However, by increasing (or decreasing in the case of negative pressure jamming) the pressure, the stiffness increases, so a stiffening behavior can be found.

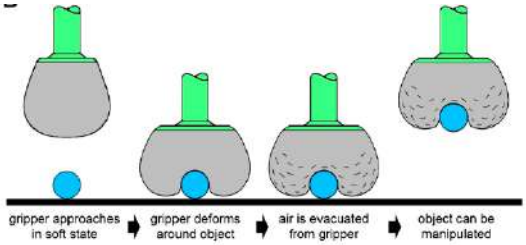

Fig. 8. Grannular jamming gripper [15]

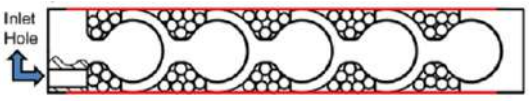

Fig. 9. Grannular jamming soft robotic spine with ball-joint [16]

1) Granular Jamming

- A simple example of granular jamming is when particles are put inside a flexible membrane. When a vacuum is applied, the granules move toward each other and the mechanism stiffens. In [15] this principle is used for a gripper as can be seen in Fig. 8. First, the membrane is put around the desired object and then a vacuum is created to stiffen the bag. With a pressure of 80 kPa inside the bag of particles, a dry surface gripping force of 37 N can be achieved. The advantage of this gripper is that it can pick up any shape as long as the gripping force is high enough to not let go of the object. So, there is no favored shape.
- In [16] a concept for a soft robotic spine with a ball joint together with granular jamming is discussed. In this concept, there are five ball joints put next to each other. Between each ball joint, granules are added and a flexible membrane is put over the whole model, see Fig. 9. The vacuum is created to deform the membrane, packing the granules around the ball joints. This concept displays a softening behavior when the pressure is kept constant while displacing the beam.
- In [17] a proposal for a potential limb support is discussed. This is based on positive pressure jamming. Instead of creating a vacuum to achieve a higher stiffness, the pressure is augmented. The design consists of a rigid outer part and a flexible internal membrane. The granules are placed in between. The pressure is increased inside the flexible membrane so the particles are blocked between the membrane and the rigid outer part, see Fig. 10. In the proposed concept several of those seen in Fig. 10 are put after each other. Between them is a self-locking joint. The stiffness is dependent on the applied pressure, the higher the pressure, the higher the stiffness.
- Instead of vacuum actuated, [14] made a tendon-driven granular jamming wrist support. The granular part of the

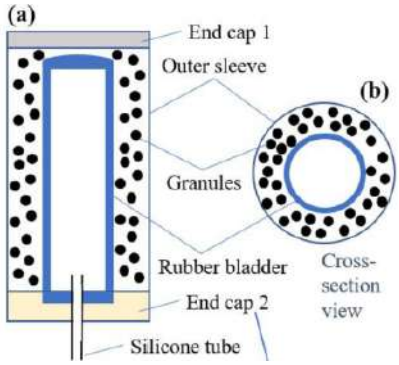

Fig. 10. Limb support application based on positive granular jamming [17]

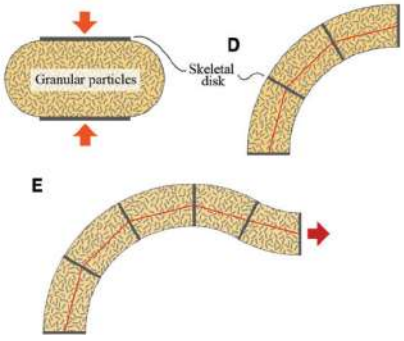

Fig. 11. Tendon driven granular jamming for wrist support [14]

wrist support is cylindrical with granules inside it and several discs to separate fragments of the cylinder, see Fig. 11. Through the disks, a tendon is placed. The disks serve a dual function: the first is to keep the tendon inside the cylinder while bending and the other is to maintain a uniform pressure on the granules. This concept is lighter and more compact compared to the vacuum-actuated designs.

- In [18] a wearable joint support was created based on negative granular jamming. The support consists of four hollow tubes that are connected to each other to maintain equal pressure throughout the system. The tubes are filled with granules and put in a circular formation. At the top and bottom of the tubes, there are two disks that keep the tubes in place. A silicon sleeve is put over the whole setup. This design exhibits a non-linear stiffness in torsion and bending and, like the other granular-based concepts, shows hysteresis.
- In [19] a soft robot is created based on granular jamming, origami, and pre-charged air. The design includes a tube consisting of the origami part on the outside. The origami can extend and compress. Inside of the tube there are three holes filled with air and a triangular hole filled with granules, see Fig. 13. When the origami structure is compressed, it presses on the air chambers increasing the pressure in the holes. With the increase in pressure in the hollow chambers, the particles are jammed together

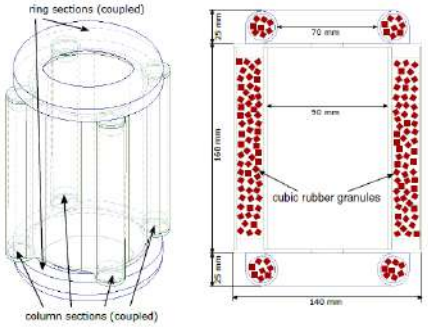

Fig. 12. Wearable joint support [18]

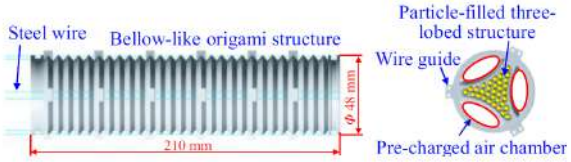

Fig. 13. Soft robot [18]

and the stiffness increases. The way the origami structure pushes on the air chambers defines the force-deflection path. So, the origami structure could be designed to achieve a certain force-deflection path. The contraction of the origami structure is activated by steel wires. Since the wires control the stiffness and the motion, the stiffness and motion are connected. This concept affects the lateral and axial stiffness.

2) Fiber Jamming

- Instead of having granules that are packed together to augment the stiffness, Brancadoro et al. tried it with cylindrical nylon fibers clamped together [13]. The same principle as for granular jamming is used, namely creating a vacuum to compress the fibers, see Fig. 14.

3) Layer Jamming

- In [20] the proposed concept is a mix of a monolithic compliant mechanism combined with negative pressure layer jamming. The compliant part is hourglass-shaped with layers placed on the top and at the bottom of it. Around this setup, there is a flexible bag. When a vacuum is created, the layers are packed together and the whole

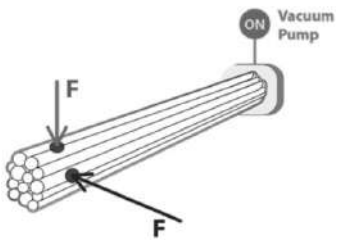

Fig. 14. Fiber jamming [13]

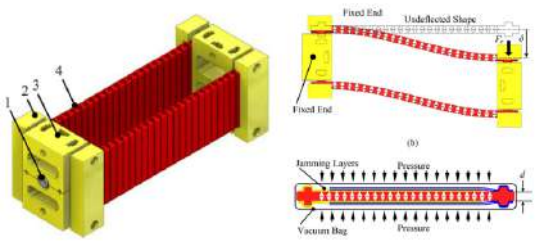

Fig. 15. Layer jamming [20]

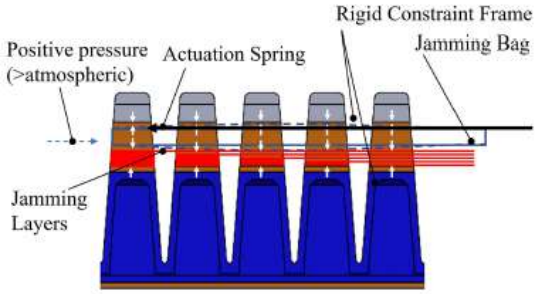

Fig. 16. Soft pneumatic gripper based on positive layer jamming [21]

system is stiffer. This system is in parallel with the same system, see Fig. 15. The advantage of having a compliant structure is the restoration of the original form once the vacuum is removed. Slip is present from 50 N at 20 mm deflection. During experiments, a stiffness ratio of 75 has been found, as well as a very short reaction time. The latter is dependent on how fast the vacuum can be achieved. This concept does require a lot of space.

- In [21] a soft pneumatic gripper was made with the principle of positive layer jamming. The gripper is made out of triangular shapes positioned next to each other to make it easy to bend in one direction and not the other. Additionally, there are layers attached at the top of the triangle. On top of those layers, there is an air-filled bag. When the pressure in the bag is increased, the layers are pushed against each other. The layers are not inside the bag. The layers are segmented as can be seen in Fig. 16. The gripper is first put in the desired shape (straight or curved) and then the pressure is increased inside the bag to increase the stiffness. For a pressure of 310 kPa a force deflection of 39 N - 6 mm was found through experimentation.

Contact-aided compliant mechanisms

Contact-aided compliant mechanisms (CACM) are mechanisms that are flexible if you bend them in a certain direction and stiff if you bend them in the other direction. The stiff direction is created by parts of the mechanism coming in contact with each other and thus obstructing further movement in the specified direction. The following concepts are mostly used for the morphing of airplane wings [6].

- The first concept discussed in [6], has non-linear stiffness only in the bending direction: low stiffness when bending in one direction and high stiffness when bending in the other direction [22]. An example can be seen in Fig. 17. When a force is applied upward of the endpoint, the material touches at the slots. When force is applied downward, the slots and the compliant hinges beneath them, permit the beam to deflect.

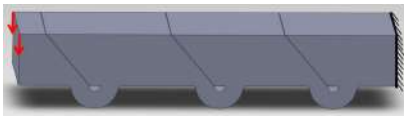

Fig. 17. Bending in one direction CACM [6]

Fig. 18. Bend and sweep CACM [6]

- The second concept discussed in [6], has non-linear stiffness in the bending and the sweeping direction. As can be seen in Fig. 18, the principle is similar to the one outlined in the previous paragraph, but now the slot is diagonal to allow bending in two directions.
- The last concept discussed in [6], incorporates non-linear stiffness in the direction of twist: flexible in counter-clockwise direction and stiff in the clockwise direction, see Fig. 19.
- In [23] a CACM for the skin of a morphing wing is discussed. As can be seen in Fig. 20 one cell of the skin consists of a compliant part with a CACM in the center. The figure demonstrates the design in a normal configuration as opposed to an auxetic configuration which is also discussed in the paper. The normal configuration is the design with a contact benefit. Even though the CACM is in the axial direction, it influences the bending stiffness. When the parts touch, the skin becomes stiffer in the direction of bending. Since those are cells that are duplicated to form a skin, this could also be placed into the metamaterial branch of shape-changing. However, since the principal cause for the non-linearity is dependent on the contact part of the mechanism as well as the selected material, it is put inside the CACM category. Note that this is the only example where no

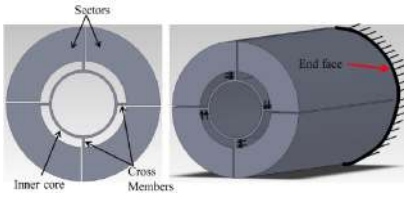

Fig. 19. Twist CACM [6]

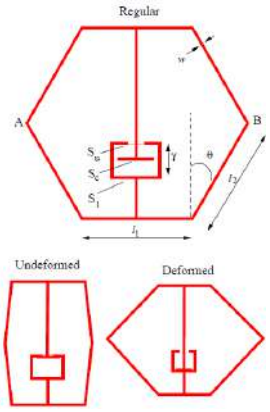

Fig. 20. Axial CACM [23]

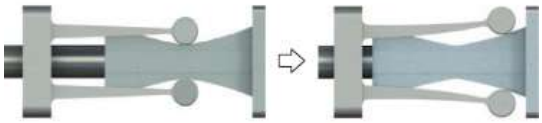

Fig. 21. Cam-follower with cam to change stiffness [24]

prototype was built, it is also the reason why it will not be evaluated in the performance table.

Cam-based designs

For the concepts based on the use of cams, several components are required, such as a cam, a cam-follower and an element that deflects. The cam has a specific shape determining the path of the cam-follower. Depending on what position the cam-follower is on the cam surface, the stiffness of the whole system varies.

- In [24] a load-adaptive actuator-powered ankle exoskeleton was made. For the actuation the stiffness was made variable with the use of two leaf springs, an hourglass-shaped cam and cam followers at the end of the leaf springs, see Fig. 21. The leaf springs have a parabolic form and are parallel to each other with the cam positioned in between the two leaf springs. When the leaf springs are moved over the cam, the direction of the force changes due to the cam form. This creates non-linear stiffness.
- In [25] the goal for non-linear stiffness applications is to have low stiffness when small loads are applied and high stiffness for high loads. This is done with a beam (cam) with a certain curvature and a ball that follows that curvature, see Fig. 22. The beam is constrained at one end and curved at the other. The curvature has the form of 1/4 of a circle and depending on the position of the contact between the roller and the beam, the direction of the force changes, which changes the stiffness.
- For a foot-ankle prosthetic, non-linear stiffness is needed since for a chosen task (normal walking, going up or down the stairs, ext.) a different stiffness is desired. The used components are a slider, a leaf spring, with one extremity attached to a cam-follower, and a cam, see Fig. 23. By rotating the ankle, the angle of the cam profile is changed. The cam-follower changes position on the cam and the leaf spring deflects. In this concept not only the cam and cam-follower change the stiffness, but also the position of the slider. The closer the slider is to the cam, the stiffer the leaf spring is, because the leaf spring is constrained in the direction of bending by the slider. The leaf spring in a deformed position stores energy and when the ankle is rotated back to its original position this energy is released [26].
- Cams are used for variable stiffness for actuators as well. The same principle of the cam and cam-follower and an elastic element to store energy are used. In [4] a torsional spring is the elastic energy storage, see Fig. 24. In [27] a linear spring is the elastic energy storage, see Fig. 25.

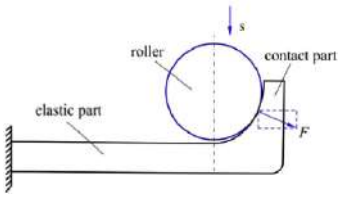

Fig. 22. Cam-follower with cam to change stiffness [25]

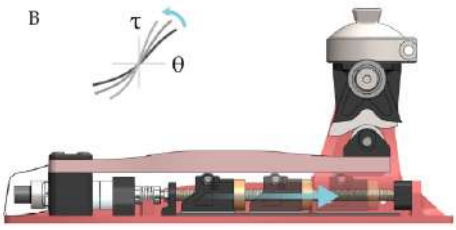

Fig. 23. Cam-follower with cam and slider to change stiffness [26]

B. Change of shape

By applying an external force, the shape of the concept changes and the stiffness changes in a non-linear way. The concepts can be subdivided in planar and spatial mechanisms, namely a concept that is designed in 2D or a concept that is designed in 3D.

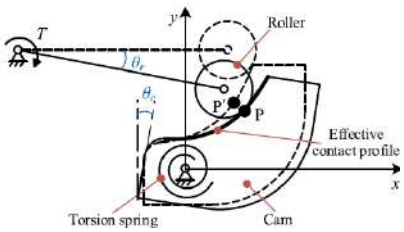

Fig. 24. Cam-follower with cam to change stiffness [4]

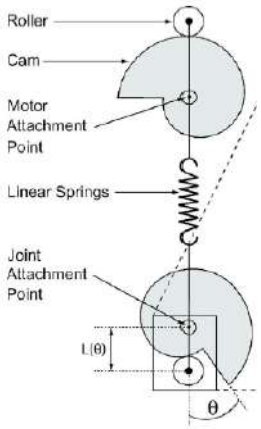

Fig. 25. Cam-follower with cam to change stiffness [27]

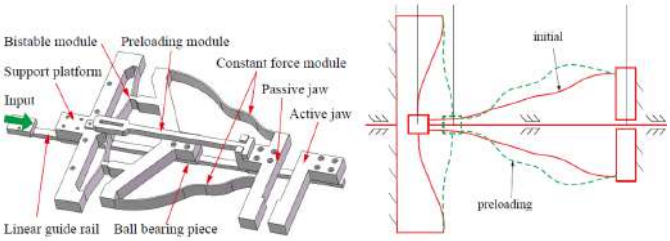

Fig. 26. Compliant gripper [28]

Planar compliant mechanism / 2D

1) Curved compliant flexures

- Zhang et al. designed a compliant gripper, see Fig. 26, with a constant force behavior for continuous deformation of objects. This gripper keeps its force constant even though the size of the grasped object changes. The gripper is made out of curved compliant flexures that form a bistable mechanism and other curved compliant flexures that form a constant force mechanism. By deforming those flexures together, they enable a constant force for a large range of motion. The average grasping force of the gripper is 8.11 N. Zhang et al. tested this gripper on a beating heart, when the size of the heart varied between 53 mm to 65 mm, the maximum fluctuation of the grasping force was 0.35 N (4.32 % of the maximum gripping force of the gripper) [28].
- In [29] compliant mechanisms with a prescribed load-displacement path were designed and made. The chosen load-displacement curves are the J-curve (stiffening), the S-curve (zero-stiffness), and the constant force curve. The designs can be found in Fig. 27, Fig. 28, and Fig. 29 respectively. All of the designs consist of one curved compliant beam. One end is attached while the other end is where the displacement force is applied. The non-linearity comes from deforming the flexures as outlined in the figures.

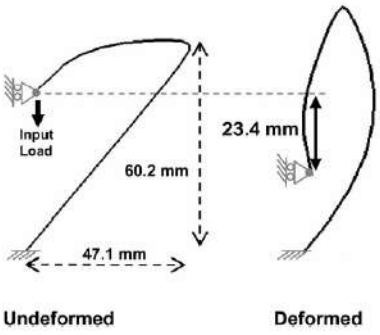

Fig. 27. J-curve non-linear spring [29]

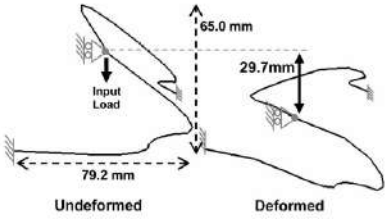

Fig. 28. S-Curve Spring [29]

2) Metamaterial

- Debeau et al. made a negative stiffness honeycomb metamaterial, this can be seen in Fig. 30. The negative stiffness comes from the elastic buckling of the compliant flexures. This concept is self-recovering, with the orignal shape in extension. When a compressive load is applied on the model, the flexures buckle elastically and the model reduces its size. Once the load is removed, the metamaterial returns to its original stretched position. The buckling of the flexures does not happen all at the same time, they buckle successively. This causes a snap-through phenomenon, which can be seen in Fig. 31 with the numbers 2,3,4 and 5 marking the end of each snap-through event. The number of snap-through events depends on the number of rows of curved beams. The magnitude of the snap-through is dependent on the selected material. Fig. 32 (a) is the force-displacement path of the design seen in Fig. 30 made in aluminum, and Fig. 32 (b) is the force-displacement path of the

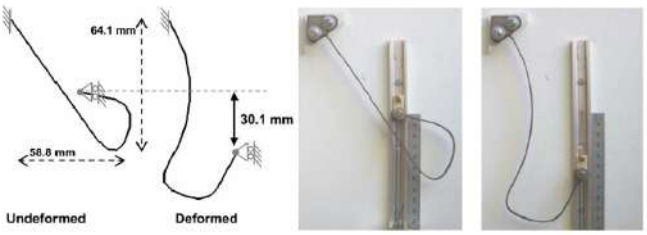

Fig. 29. Constant force spring [29]

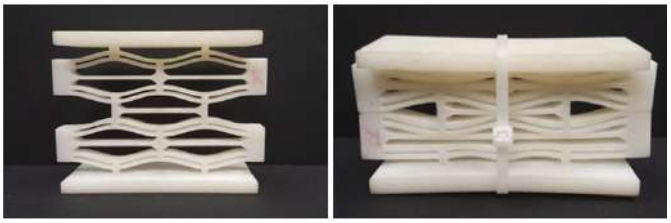

Fig. 30. Original and compressed shape of metamaterial [30]

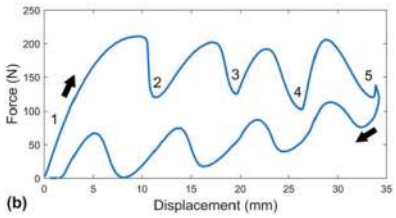

Fig. 31. Force-displacement curve, snap-through and hysteresis phenomenons of metamaterial [30]

same design but made with nylon. The major difference in behavior between the two materials is that magnitude in the snap-through is lower for aluminum than for nylon. The aluminum design behaves as a constant force characteristic. The number of columns however is proportional to the magnitude of the force threshold for the buckling of the flexures. Another phenomenon that is present is hysteresis. So when the compressive load is removed, there is a dissipation of the energy that was stored in the buckling of the flexures [30].

- Rafsanjani et al. analyzed how to tune the non-linear

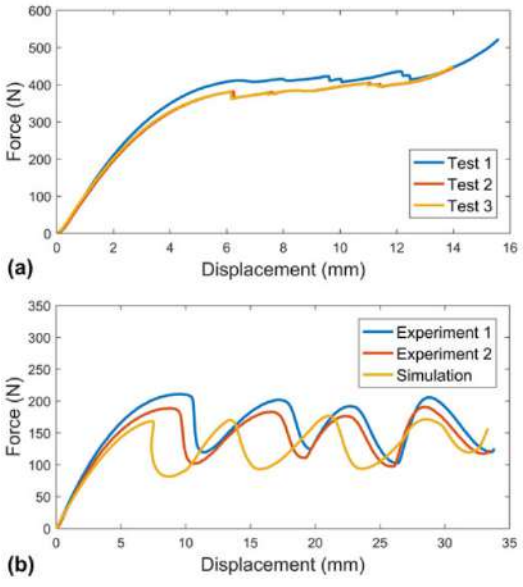

Fig. 32. Experimental force-displacement curve metamaterial, (a) with aluminium and (b) with nylon [30]

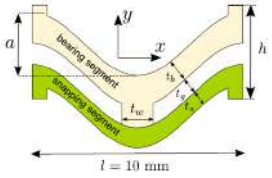

Fig. 33. Unit-cel metamaterial, white is stiff part and green is flexible part [31]

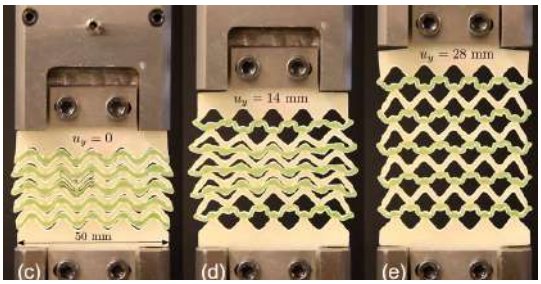

Fig. 34. Metamaterial [31]

behavior, such as monotonic, S-shaped, plateau, and non-monotonic snap-through behavior of metamaterials. The design is in its original configuration wavvy and when an extensive load is applied, the design is diamond-shaped. This can be seen in Fig. 34. A figure of the unit cell can be seen in Fig. 33, with the white part being the stiff part (not deforming under pressure) and the green part being the deformable part. The ratio of a/l changes the stiffness behavior. For a ratio of a/l = 0.2 there is no snap-though event. As the ratio increases, so does the number of snap-through events, again this depends on the number of rows in the concept. This concept can be used in vibration isolation and damping applications [31].

- In [32] two different snap-through metamaterials are discussed. Those can be seen in Fig. 35 and Fig. 36. Depending on the specific dimensions the concepts do not have a snap-through, are self-recovering or are multi-stable. The principles are already explained in the previous paragraphs.

Shell mechanism / 3D

- For a wearable arm support, non-linear stiffness is desired, since the support needed depends on how high the arm is lifted. The concept is based on a tape spring and limits the maximal support to 25 % to avoid deterioration of the arm muscles. This is a shell mechanism with a single-curved surface. When a certain force threshold is applied, the tape spring buckles and the curved surface becomes flat. That buckling reduces the stiffness and demonstrates a softening behavior. When the arm is at rest next to the body, the arm support is buckled, which can be seen in Fig. 37. This concept has a range of motion of 100°, which is necessary for arm mobility [33].
- [34] uses the same principle as [33] to achieve non-linear stiffness, but has a constant force curve instead of

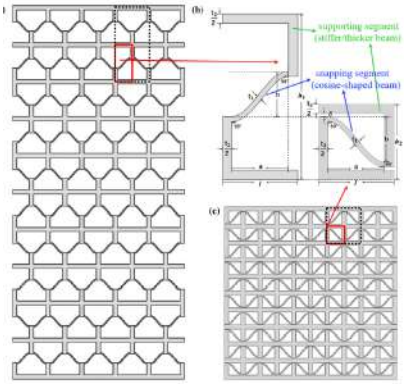

Fig. 35. Metamaterial [32]

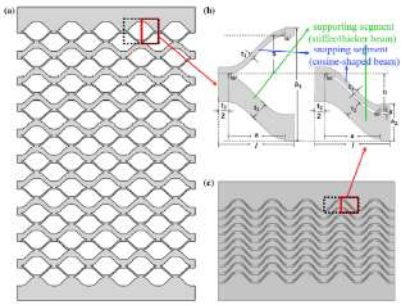

Fig. 36. Metamaterial [32]

softening. The difference between the two concepts is the planar cut-out, which can be seen in Fig. 38. [34] is used for gravity-balanced compliant shell mechanisms.

- In [35] a shell mechanism based on a carnivorous plant is proposed. The concept consists out of two curved shells, which can be seen in Fig. 39. The intersection of those two shells forms the compliant hinge of the entire model. When applying load on the extremities of the shells, the mechanism closes and shows a stiffening behavior.
- In [36] negative torsional stiffness is achieved by means of three curved flexures. These are all placed in a circle and attached at their endpoints to two discs, see Fig. 40. The bottom disc is constrained in all directions and the upper disc can rotate with respect to its own axis. While rotating the compliant strips have large deformation but do not buckle. The non-linearity comes from the force arm that continuously decreases while rotating one of the two discs. In the initial configuration, the curved beams have some prestress. The paper also mentions that if those strips do not have prestress similar negative stiffness behavior is expected.

Fig. 37. Prototype arm support [33]

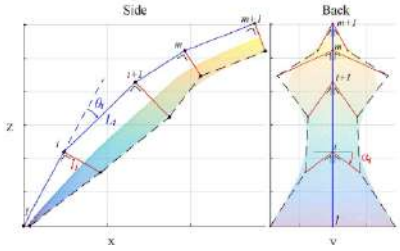

Fig. 38. Gravity balancer, side and back view [34]

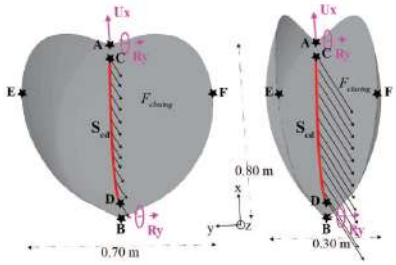

Fig. 39. Open and closed configuration of shell mechanism [35]

C. Material properties

Another aspect that can influence the stiffness of designs is the choice of material. Rubber and aluminum could both be used for the same model, but would have a very different stiffness behavior outcome. In this paper, the focus will not be on material properties; however, one example is given.

- In [37] several materials are used to create a certain stiffness behavior. This concept is designed to be used in morphing air wings. The primary investigated material is a hyper-elastic ”skin” material, with a fracture strain of 364 %.

Fig. 40. Torsional negative stiffness concept [36]

TABLE I
PERFORMANCE OVERVIEW

Work	Category	Type of stiffness	Range of motion, max	Strength, max	Weight/size	Size-Force efficiëncy	Number of parts	Direction of stiffness
[8]	BC: State based: initial prestress	Softening/ negative	90°	25 Nm	1778 cm^3 0.600 kg	0	0	Torsional
[9]	BC: State based: initial prestress	Stiffening	5°	6 Nm	*	*	+	Extension spring
[10]	BC: State based: initial prestress	Stiffening → negative	120°, 0.075m	30 Nm-50 Nm (pretension dependent)	8 kg	0	+	Extension spring
[11]	BC: State based: other	Dependent on placement and length bellow	1 m	*	23.362 cm^3 0.04244 kg	*	+	Bending and torsional
[12]	BC: State based: other	Dependent on placement spindle	2*r, deflection spring: 134 mm	*	*	*	-	Extension spring
[15]	BC: Jamming: granular	Softening @ 80 kPa pressure	Dry surface: 2.7 mm Wetsurface: 3.6 mm	37 N 42 N	333 cm^3	++	+	Unspecified
[10]	BC: Jamming: granular	Softening @ -60 kPa Softening @ -90 kPa	33 mm 13 mm	3.5 N 3.5 N	105 cm^3	-	+	Bending
[17]	BC: Jamming: granular	Softening @ 62 kPa Softening @ 172 kPa	11 mm 12 mm	4.5 N 23 N	106 cm^3	+	++	Bending
[14]	BC: Jamming: granular	Softening	10 mm	6N	184 g	0	++	Bending
[18]	BC: Jamming: granular	Softening @ 20 kPa pressure	Bending: 32° Axial: 48°	1.5 Nm 0.43 Nm	1900 cm^3	–	+	Bending and torsional
[19]	BC: Jamming: granular	Stiffening @ 20 kPa Stiffening @ 40 kPa	Bending: 55 mm Axial: 22 mm	13 N 90 N	380 cm^3	+	++	Bending and axial
[13]	BC: Jamming: fiber	Softening	CT : 45 mm BT: 45 mm FBT: 45mm	4.77 N 3.94 N 4.06 N	130 cm^3	-	++	Bending
[20]	BC: Jamming: layer	Softening @ -86 kPa	20 mm	42 N	1300 cm^3	–	++	Bending
[21]	BC: Jamming: layer	Softening @ 310 kPa	6 mm	39 N	55 cm^3	++	++	Bending
[6]	BC: CACM	Stiff and soft direction	-20 % → 3 %	-100 N→75 N	*	*	–	Bending
	BC: CACM	Stiff and soft direction	Sweep: -15 % → 3 % Bend: -37 %→5 %	-150 N→150 N -150 N→150 N	*	*	-	Bending 2D
	BC: CACM	Stiff and soft direction	CW→CCW -14°→23°	Stress 20 MPa→10 MPa	*	*	–	Torsional
[24]	BC: Cam based	Stiffening	17 mm	800 N	0.77 kg in total	*	-	Bending cam follower
[25]	BC: Cam based	Stiffening	1.7 °	12 Nm	0.5 cm^3	++	–	Bending cam follower
[26]	BC: Cam based	Stiffening	*	90 Nm	625 cm^3 578 g	++	–	Torsional
[4]	BC: Cam based	Stiffening	2°	22 Nm	*	*	–	Extension spring
[28]	Change of shape: planar monolithic flexures	Constant force	20 mm	8.11 N	540 cm^3	-	–	Bending
[29]	Change of shape: planar monolithic flexures	Stiffening S-curve Constant force	ex 1: 23 mm ex 2: 30 mm ex 3: 60 mm	11 N 6.5 N 9 N	11 cm^3 21 cm^3 18 cm^3	+	–	Bending
[30]	Change of shape: planar metamaterial	Softening Negative stiffness	Aluminium: 14 mm Nylon: 32 mm	380 N 180 N	15.5 cm^3 14.8 cm^3	++	–	Axial
[31]	Change of shape: planar metamaterial	Negative stiffness => stiffening	ex 1: 1.05 strain ex 2: 1.2	6 MPa→900 N 3 MPa→450 N	*	*	–	Axial
[32]	Change of shape: planar metamaterial	Negative stiffness	OUM: 1.05→136 mm PUM: 2.5→136 mm	0.03 MPa Stress 0.01 MPa	72→145 cm^3 31→102 cm^3	*	–	Axial
[33]	change of shape: spatial	Softening	100°	1.6 Nm	180 cm^3	+	0	Bending
[34]	change of shape: spatial	Constant force	500 mm	0.1 N	40 cm^3	-	0	Bending
[35]	change of shape: spatial	Stiffening	140 mm	50 N	120 cm^3 432 g	+	-	Unspecified
[36]	change of shape: spatial	Negative stiffness	180°	4 dimensionless momentarm	*	*	-	Torsional
[37]	material properties	Softening	35° chordwise	7 N	*	*	++	Unspecified

TABLE II
GAPS IN LITERATURE

Second branch	Torsional Stiffness	Bending Stiffness	Axial Stiffness	Unspecified Stiffness
State based	2	1	3	*
Jamming	1	8	1	1
CACM	1	3	*	*
Cam based design	1	2	1	*
Change of shape	1	4	3	1

IV. PERFORMANCE OVERVIEW

In this section, a performance overview of the discussed concepts will be offered. Performance is judged based on relevant criteria for non-linear stiffness. The three most important criteria for non-linear stiffness are a certain mechanism's maximum strength, range of motion and characteristic force-deflection path. Other relevant criteria include the weight or size of the mechanism, the number of parts of the mechanism, and the direction of the non-linear stiffness. These are further explained below.

Type and direction of stiffness: For every application, it is necessary to know what type of stiffness is needed, as well as its direction.

Range of motion: One of the disadvantages of a compliant mechanism is the lack of large range of motions. For example, it is not possible to have a compliant hinge that is capable of a 360° rotation. Thus, the range of motion is evaluated either with the degree the mechanism can rotate or the displacement it has in the bending or axial direction.

Strength: Strength is also an important factor for some applications. For exoskeletons, for example, it is important to know how much support a mechanism can provide. Similarly, for minimally invasive surgery, it is essential to know how much gripping force can be given by the mechanism.

Weight and size: In most applications, it is desirable to minimize the weight and size of components. This criterion provides insight into the relational difference in the size of various designs. However, when looking at the maximum force, weight should be taken into account, as heavier or larger mechanisms have a tendency of achieving higher forces or moment arms. That is why the size-strength efficiency is part of the evaluation.

Number of parts: When designing mechanisms the number of parts is minimized. The more parts, the more the concept is considered complex. The complexity of [8] is taken as an average and receives a "0" in the table. The concepts that have relatively more parts receive a "+" in the table. Designs with even more parts receive a "++". However, if the concept has fewer parts it receives a "−" or even a "−−".

In Table I the performance overview can be found. Some boxes are colored. Those colors are the confidence level of the information written inside. Red means no information is given. Orange means some information is given, but the certainty of the value given is not certain. Green is the highest confidence level, where the information is exactly stated in the paper. It should be noted that for the weight/size part in the table, the size is given of 1 part of the mechanism, so for a gripper only one arm, for 3 torsion bars only the weight of 1 torsion bar, etc.

V. DISCUSSION

This paper aims to give an overview of the different concepts that couple stiffness non-linearity to their motion. In the following paragraphs, a reflection on the existing solutions is provided.

First, this categorization is based on what makes a specific concept exhibit a non-linear stiffness. This is to create an overview of the possibilities of incorporating non-linearity in compliant mechanisms. However, an alternative categorization could have been made based on the type of stiffness or the type of force-displacement path. In the current categorization, some concepts could be placed in multiple branches. In those cases, the main design reason for the non-linearity is chosen as a branch of the concept.

There can be no certainty that all existing relevant papers are included in this review, as different terms for the same subject are used, thus such papers using alternative terms may not be included.

Overall, the jamming solutions need the most parts and are thus the most complex and spacious. These designs require an additional external source to modify their force-displacement path. Mostly a pressure pump is needed, which further increases complexity. The concepts that achieve the highest strength are layer jamming as they have the most friction. These have the most capability to change the force-deflection curve. More research has been conducted on granular and layer jamming as opposed to fiber jamming. Almost all jamming solutions have a softening behavior coupled to their motion but a stiffening behavior if the pressure is changed, which is considered a variable stiffness since it can be altered on demand.

The concept solutions able to achieve the highest moments and forces are the cam-based solutions, all of which use springs, so they have a compliant part. However, these concepts could not be directly designed to be made monolithic. A lot of parts are needed for those solutions and the range of motion is low in comparison to the other concepts.

The category of shape-changing is the one that has the largest range of motion. The change of shape has the highest possibility of having the desired force-deflection path, with the least necessary parts. This category is also the easiest to manufacture, especially the planar concepts, as these can be 3D printed or laser-/ water cut. The spatial solutions are typically more difficult to produce since they are built in a 3D shape, but depending on the design this can be easier or more difficult to manufacture. Curved compliant flexures show a non-linear behavior in bending stiffness. To achieve non-linear behavior in axial stiffness, metamaterials are a more appropriate choice.

CACMs are used for non-linear stiffness in bending stiffness and torsional stiffness [6]. However, there is a gap in the axial stiffness. Some CACMs can extend or compress due to contact, but only to change the bending stiffness, thus these are mostly used in morphing air wings [23]. In [23] the axial stiffness changes thus it could be considered as a bistable mechanism, but the focus of this paper is not its axial stiffness.

The only concepts that can have negative stiffness are based on pre-stress and change of shape, for example as a result of buckling.

As can be seen in Table II all the branches have a concept for torsional, bending, and axial stiffness except CACMs in the axial direction, as previously explained.

VI. Conclusion

This paper's goals are twofold: (i) to give an overview of compliant structures that have a non-linear stiffness coupled to their motion with a prototype built to confirm the working principle and (ii) to compare the different concepts by providing a performance overview.

Regarding the first goal, all papers have a non-linear stiffness coupled to their motion and all but one paper has a working prototype. An overview of the concepts is presented in all papers by a tree diagram which classifies the papers into 3 main branches: the change in boundary conditions, the change of shape and the change of material properties. All papers could be inserted in the diagram in a specific branch. However, some papers could belong to multiple branches.

For the second goal, a comparison of compliant mechanisms which have a non-linear stiffness is given. This comparison is based on the range of motion, maximum strength, weight and size, size-strength efficiency, complexity, and type of and direction of stiffness. These categories give a clear overview of the advantages and disadvantages of the discussed mechanisms.

The jamming solutions are the largest and most complex. These have two types of non-linear behavior; their softening behavior is motion linked and their stiffening behavior can be changed on demand. CACMs' stiffnesses are dependent on the load direction, and their non-linearity is difficult to tune. The cam-based solutions can achieve the highest moments and forces, whilst shape-changing has the largest range of motion.

Further work should be done on calculating the size-strength efficiency since 12 out of the 31 proposed concepts do not indicate this value. Furthermore, only 9 concepts are considered efficient or very efficient based on the criteria mentioned in Section IV. Therefore, more concepts with a high size-strength efficiency should be developed. The next step would be to make concepts with high size-strength efficiency combined with a large range of motion. Additionally, to fill the gap, a CACM focussing on its non-linear axial stiffness should be created.

References

[1] L. L. Howell, "Compliant mechanisms," in *21st Century Kinematics*, J. M. McCarthy, Ed. London: Springer London, 2013, pp. 189–216.

[2] S. Barbarino, O. Bilgen, R. Ajaj, M. Friswell, and D. Inman, "A review of morphing aircraft," *Journal of Intelligent Material Systems and Structures - J INTEL MAT SYST STRUCT*, vol. 22, 08 2011.

[3] L. Blanc, A. Delchambre, and P. Lambert, "Flexible medical devices: Review of controllable stiffness solutions," *Actuators*, vol. 6, no. 3, 2017. [Online]. Available: https://www.mdpi.com/2076-0825/6/3/23

[4] X. Hu, Z. Song, and T. Ma, "Novel design method for nonlinear stiffness actuator with user-defined deflection-torque profiles," *Mechanism and Machine Theory*, vol. 146, p. 103712, 04 2020.

[5] L. Staats, "Stiffness reduction of cantilever i-beams through lateral torsional buckling for compliant beams," Master's thesis, Delft University of Technology, 2021. [Online]. Available: http://resolver.tudelft.nl/uuid:2f994423-ff74-4ac3-bde1-b009cf6b5113

[6] Y. Tummala, "Design and optimization of contact-aided compliant mechanisms with nonlinear stiffness," Ph.D. dissertation, The Pennsylvania State University, 2013.

[7] T. E. Bruns and D. A. Tortorelli, "Topology optimization of non-linear elastic structures and compliant mechanisms," *Computer Methods in Applied Mechanics and Engineering*, vol. 190, no. 26, pp. 3443–3459, 2001. [Online]. Available: https://www.sciencedirect.com/science/article/pii/S0045782500002784

[8] G. Radaelli, "Synthesis of mechanisms with prescribed elastic load-displacement characteristics," Ph.D. dissertation, Delft University of Technology, 2017.

[9] F. Petit, M. Chalon, W. Friedl, M. Grebenstein, A. Schäffer, and G. Hirzinger, "Bidirectional antagonistic variable stiffness actuation: Analysis, design implementation," 06 2010, pp. 4189 – 4196.

[10] I. Thorson and D. Caldwell, "A nonlinear series elastic actuator for highly dynamic motions," 09 2011, pp. 390–394.

[11] A. Amoozandeh, G. Radaelli, W. van de Sande, R. Ostayen, and J. Herder, "Characterization of spatially curved beams with anisotropically adaptive stiffness using sliding torsional stiffeners," *International Journal of Mechanical Sciences*, vol. 234, p. 107687, 08 2022.

[12] W. Dorsser, R. Barents, B. Wisse, M. Schenk, and J. Herder, "Energy-free adjustment of gravity equilibrators by adjusting the spring stiffness," *Proceedings of The Institution of Mechanical Engineers Part C-journal of Mechanical Engineering Science*, vol. 222, pp. 1839–1846, 09 2008.

[13] M. Brancadoro, M. Manti, S. Tognarelli, and M. Cianchetti, "Fiber jamming transition as a stiffening mechanism for soft robotics," *Soft Robotics*, vol. 7, 04 2020.

[14] J. Choi, D.-Y. Lee, J.-H. Eo, Y. J. Park, and K.-J. Cho, "Tendon-driven jamming mechanism for configurable variable stiffness," *Soft Robotics*, vol. 8, 06 2020.

[15] E. Brown, N. Rodenberg, J. Amend, A. Mozeika, E. Steltz, H. Lipson, and H. Jaeger, "Universal robotic gripper based on the jamming of granular material," *Proceedings of the National Academy of Sciences of the United States of America*, vol. 107, 10 2010.

[16] Y. Wei, y. Chen, Y. Yang, and Y. Li, "A soft robotic spine with tunable stiffness based on integrated ball joint and particle jamming," *Mechatronics*, vol. 33, 12 2015.

[17] T. Liu, H. Xia, D.-Y. Lee, A. Firouzeh, Y.-L. Park, and K.-J. Cho, "A positive pressure jamming based variable stiffness structure and its application on wearable robots," *IEEE Robotics and Automation Letters*, vol. 6, pp. 8078–8085, 10 2021.

[18] S. Hauser, M. Robertson, A. Ijspeert, and J. Paik, "Jammjoint: A variable stiffness device based on granular jamming for wearable joint support," *IEEE Robotics and Automation Letters*, vol. PP, pp. 1–1, 01 2017.

[19] Y. Li, T. Ren, y. Chen, and M. Chen, "A variable stiffness soft continuum robot based on pre-charged air, particle jamming, and origami," 05 2020, pp. 5869–5875.

[20] X. Zeng, C. Hurd, H.-J. Su, S. Song, and J. Wang, "A parallel-guided compliant mechanism with variable stiffness based on layer jamming," *Mechanism and Machine Theory*, vol. 148, p. 103791, 06 2020.

[21] G. Crowley, X. Zeng, and H.-J. Su, "A 3d printed soft robotic gripper with a variable stiffness enabled by a novel positive pressure layer jamming technology," *IEEE Robotics and Automation Letters*, vol. 7, pp. 1–1, 04 2022.

[22] Y. Tummala, A. Wissa, M. Frecker, and J. Hubbard Jr, "Design and optimization of a contact-aided compliant mechanism for passive bending," *Journal of Mechanisms and Robotics*, vol. 6, p. 031013, 06 2014.

[23] V. Mehta, M. Frecker, and G. Lesieutre, "Contact-aided compliant mechanisms for morphing aircraft skin," in *Modeling, Signal Processing, and Control for Smart Structures 2008*, D. K. Lindner, Ed., vol.

6926, International Society for Optics and Photonics. SPIE, 2008, p. 69260C. [Online]. Available: https://doi.org/10.1117/12.773599

[24] Y. Shao, W. Zhang, Y. Su, and X. Ding, "Design and optimisation of load-adaptive actuator with variable stiffness for compact ankle exoskeleton," *Mechanism and Machine Theory*, vol. 161, p. 104323, 07 2021.

[25] Z. Song, S. Lan, and J. Dai, "A new mechanical design method of compliant actuators with non-linear stiffness with predefined deflection-torque profiles," *Mechanism and Machine Theory*, vol. 133, pp. 164–178, 03 2019.

[26] M. Shepherd and E. Rouse, "The vspa foot: A quasi-passive ankle-foot prosthesis with continuously variable stiffness," *IEEE transactions on neural systems and rehabilitation engineering : a publication of the IEEE Engineering in Medicine and Biology Society*, vol. PP, 09 2017.

[27] S. Migliore, E. Brown, and S. Deweerth, "Novel nonlinear elastic actuators for passively controlling robotic joint compliance," *Journal of Mechanical Design - J MECH DESIGN*, vol. 129, 04 2007.

[28] Q. Zhang, P. Liu, and P. Yan, "Design and test of a curved-beam based compliant gripper for manipulations of actively deformable objects," *IEEE Access*, vol. PP, pp. 1–1, 01 2022.

[29] C. Jutte and S. Kota, "Design of nonlinear springs for prescribed load-displacement functions," *Journal of Mechanical Design - J MECH DESIGN*, vol. 130, 08 2008.

[30] D. Debeau, C. Seepersad, and M. Haberman, "Impact behavior of negative stiffness honeycomb materials," *Journal of Materials Research*, vol. 33, pp. 290–299, 02 2018.

[31] A. Rafsanjani, A. Akbarzadeh, and D. Pasini, "Snapping mechanical metamaterials under tension," *Advanced Materials*, vol. 27, p. 5931, 10 2015.

[32] H. Yang and L. Ma, "Multi-stable mechanical metamaterials by elastic buckling instability," *Journal of Materials Science*, vol. 54, 02 2019.

[33] S. van der Kemp, "Design of a compact wearable arm support utilizing shape optimized shell mechanisms: To be worn underneath the surgical gown," Master's thesis, Delft University of Technology, 2018. [Online]. Available: http://resolver.tudelft.nl/uuid:3664c6fd-da05-48b5-a503-a9e373d912a0

[34] G. Radaelli and J. Herder, "Gravity balanced compliant shell mechanisms," *International Journal of Solids and Structures*, vol. 118-119, 04 2017.

[35] V. Charpentier, S. Adriaenssens, and O. Baverel, "Large displacements and the stiffness of a flexible shell," *International Journal of Space Structures*, vol. 30, pp. 287–296, 12 2015.

[36] J. Li, K. Fu, Y. Gu, and Z. Zhao, "Torsional negative stiffness mechanism by thin strips," *Theoretical and Applied Mechanics Letters*, vol. 9, no. 3, pp. 206–211, 2019. [Online]. Available: https://www.sciencedirect.com/science/article/pii/S2095034919300364

[37] L. Xiao, H. Zhao, Z. Xu, X. Li, C. Shen, K. Wang, and L. Zhang, "A new architecture of morphing wing based on hyperelastic materials and metastructures with tunable stiffness," *Frontiers in Mechanical Engineering*, vol. 7, 02 2022.

3

Research paper

The use of contact-release of torsional beams in an open chain for a softening behavior

S.S.L. Koentges
Faculty of Mechanical, Maritime and Materials Engineering
Delft University of Technology
Delft, Zuid-Holland

***Abstract*—This study aims to achieve a softening moment-angle response by utilizing compliant parts. The approach uses the principle of contact release, which involves initially prestressed torsional bars arranged in series, separated by rigid bodies. By stepwise activation of the torsional bars, a softening behavior is achieved. Mechanical stops are employed to maintain the initial prestress. A Pseudo Rigid Body Model (PRBM) is developed to calculate the moment-angle behavior of the complete prototype. The optimization of the PRBM is performed using a cost function based on the least square error. The optimization parameters are the stiffness of the torsional bars and their initial prestress. Additionally, a Finite Element Analysis (FEA) is conducted to analyze the behavior of an individual I-profile torsional bar. Experimental validation of both the PRBM and the FEA models is carried out using a prototype. The prototype is constructed based on the results obtained from the PRBM optimization to follow the desired graph closely. The results from both FEA and PRBM align closely with the predicted curves, confirming the effectiveness of the proposed approach.**

***Index Terms*—Compliant Mechanisms, Softening Behavior, Contact-Release, Non-Linear Stiffness**

I. Introduction

Compliant Mechanisms (CMs) offer a promising alternative to traditional rigid body mechanisms by using the elastic deformation of flexible parts for movement. They provide advantages such as reduced wear, lower backlash, fewer parts, and reduced mass compared to their rigid counterparts. However, these mechanisms also have limitations, including limited range of motion, fatigue susceptibility, and design complexity [1]. Additionally, CMs can exhibit non-linear behavior, which have found positive applications in aerospace engineering, medical devices, and soft robotics.

Softening behavior, characterized by a decreasing stiffness with increasing deformation, has gained significant attention in various engineering applications, including soft robotics, exoskeletons, and static balancers. In exoskeletons, the non-linear response is essential for optimal support during user-device interactions. It is important to emphasize that while this paper focuses on softening behavior, there are noteworthy innovations that explore contrasting stiffening behavior. These concepts use torsional bars arranged in series and employ the contact release principle to achieve a stiffening response, primarily designed for vehicle suspensions [2, 3]. In addition to using torsional beams for stiffening behavior, other concepts within the same field use torsional bars to achieve softening behavior. For instance, van Nes' work focused on a closed-chain static balancer using torsional springs with linear or non-linear characteristics and prestressed or relaxed torsional springs [4]. Nevertheless, he did not consider compliant parts or construct a prototype using the contact release principle. Additionally, Claus developed a static balancer for a foldable container, simplifying it to an inverted pendulum. His work introduced a concept of two torsional bars arranged in parallel with one mechanical stop to achieve a softening behavior [5]. His concept focuses on only two torsional bars and does not include the possibility of using more bars in parallel. Similarly, Radaelli investigated a gravity balancer using contact release of torsional springs, with multiple torsional springs positioned along the same torsional axis [6]. However, the design did not incorporate compliant mechanisms.

This paper presents a novel approach that utilizes compliant torsional beams in an open chain with the contact release principle. The mechanism's movement solely relies on the elastic deformation of the torsional beams arranged in series and separated by rigid bodies. The objective is to achieve a range of motion of 120° and a desirable softening behavior. The research methodology involves a combination of the development of a Pseudo Rigid Body Model (PRBM) to simulate the behavior of the complete concept, an optimization process to adjust the stiffness and initial prestress of the torsional beams in the PRBM, and a Finite Element Analysis (FEA) on an I-beam to determine the stress-levels. The findings from the PRBM simulations, and experimental results of the prototype are compared.

The structure of this paper is as follows: Section 2 presents the working principle of the concept and details the research methodology, including the PRBM development, FEA analysis, and experimental validation. Section 3 provides the results obtained from simulations and experiments. Section 4 discusses the implications of the findings and proposes avenues for future research. Finally, Section 5 concludes the paper by summarizing this study's key findings and contributions.

II. Method

Section II-A explains the concept's working principle. The PRBM is introduced in Section II-B, providing insights into the simulated moment-angle behavior and movement of the complete concept. Furthermore, an optimization process is applied to the PRBM, allowing for the adjustment of multiple

parameters. Subsequently, the FEA for a single torsional I-beam is discussed in Section II-C. The outcomes of the PRBM optimization guide the fabrication of a prototype, as detailed in Section II-D. Experimental verification is conducted on the prototype to validate the accuracy and reliability of both the PRBM and the FEA, as presented in Section II-E.

A. Working principle

The total stiffness for springs in series is calculated by:

$$k_{tot} = \left(\sum_{i=1}^{N} \frac{1}{k_i} \right)^{-1}$$

k_{tot} denotes the stiffness of the entire system, k_i represents the stiffness of individual springs, and N is the total number of springs. It is important to note that the overall stiffness of springs in series is always lower than that of the softest spring in the series.

The principle of contact release can be explained using Fig. 1. In situation (a), two tension springs are arranged in series. The first spring's endpoint is fixed, while a load is applied at the endpoint of the second spring. The orange square in the illustration indicates the attachment point between the two springs. When a load F is exerted, both springs extend, resulting in a total stiffness of $k_{tot} = (\frac{1}{k_1} + \frac{1}{k_2})^{-1}$. It is assumed that the stiffness is linear. Situations (b), (c), and (d) involve the prestressing of the first spring and the addition of mechanical stops, depicted as pink-colored elements in the image. These stops prevent the orange attachment point from returning to the relaxed position of the first spring but allow the second spring to extend further. When a load is applied, initially only the second spring extends since the load is lower than the first spring's prestress. The total stiffness is then calculated as $k_{tot} = k_2$ as is the case in situations (b) and (c). Only when the external load exceeds the prestress of the first spring will the orange square disengage from the pink mechanical stops, enabling the extension of the first spring, as in situation (d). At this point, the total stiffness matches the situation in (a), resulting in $k_{tot} = (\frac{1}{k_1} + \frac{1}{k_2})^{-1}$. As the figure demonstrates, situations (a) and (d) exhibit the same slope. Additionally, situations (b)-(d) represent the contact release principle and demonstrate a softening behavior.

In the context of this paper, torsional springs are employed instead of linear springs. For illustration, consider a configuration where three torsional springs are connected in series, all initially prestressed. The prestress of the first spring is lower than that of the second spring, and the second spring's prestress is lower than that of the third spring. Fig. 2 visualizes the initial collinear configuration, with circles representing the torsional springs, lines denoting the connecting rigid bodies, and various colors indicating different positions of the system, with the green color being the unprestressed configuration. The leftmost rigid body is fixed at the coordinates (0,0), and the other side of the same rigid body is connected to the first spring. When a counterclockwise moment is applied at the right end of the rightmost rigid body, the mechanism remains

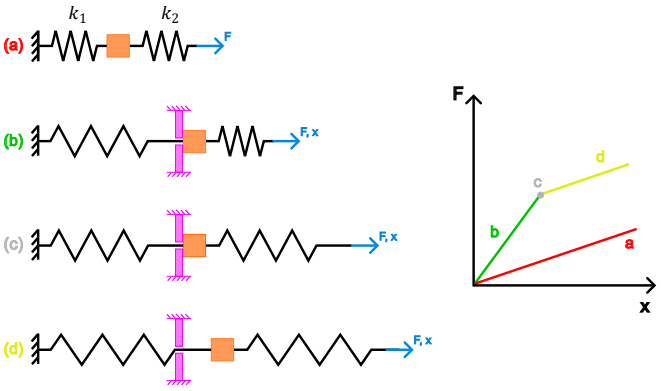

Fig. 1. Softening behavior with prestressed elements. The orange square connects the two springs, and the pink rectangles are mechanical stops creating the first springs' prestress. (a) No prestress and $k_{tot} = (\frac{1}{k_1} + \frac{1}{k_2})^{-1}$, (b) $Fx <$ prestress and $k_{tot} = k_2$, (c) $Fx =$ prestress and $k_{tot} = k_2$, (d) $Fx >$ prestress and so $k_{tot} = (\frac{1}{k_1} + \frac{1}{k_2})^{-1}$.

stationary until the applied moment exceeds the prestress of the first spring. This corresponds to the blue line in Fig. 2 and the blue line on the moment-angle graph in Fig. 3. Once this threshold is surpassed, the first spring loses contact and initiates movement, while the second and third springs maintain contact with their mechanical stops. This corresponds to position 'b' in both figures. On the moment-angle graph, this is depicted by the red line, with the total stiffness equal to the stiffness of the first spring alone. As the moment further increases, the first spring continues to move, and upon reaching the prestress threshold of the second spring (situation 'c' in both figures), the second spring is also activated. The total stiffness of the mechanism becomes the combined stiffness of the first and second springs in series, resulting in $k_{tot} = (\frac{1}{k_1} + \frac{1}{k_2})^{-1}$. Subsequently, when the moment surpasses the prestress threshold of the third spring (situation 'd' in both figures), the third spring loses contact and becomes activated. This leads to a further decrease in the overall stiffness of the system, now given by $k_{tot} = (\frac{1}{k_1} + \frac{1}{k_2} + \frac{1}{k_3})^{-1}$. Thus, the entire system's stiffness decreases upon each spring's activation, resulting in a softening behavior.

The selected concept consists of a series of torsional bars. Each torsional bar is initially torsionally prestressed and mechanically blocked. The activation of each torsional bar occurs sequentially, one at a time. With the activation of each torsional bar, a spring is introduced to the system, resulting in a softening behavior.

B. PRBM

The PRBM aims to determine the moment-angle characteristics and simulate the system's movement. This approach simplifies the concept by using serially connected springs and rigid parts, considering a 2D configuration. Fig. 4 illustrates this, with the blue line depicting a certain system position. The circles in the figure represent the springs, also called nodes. The system is fixed at the coordinate (0,0), imposing constraints on all three DOFs.

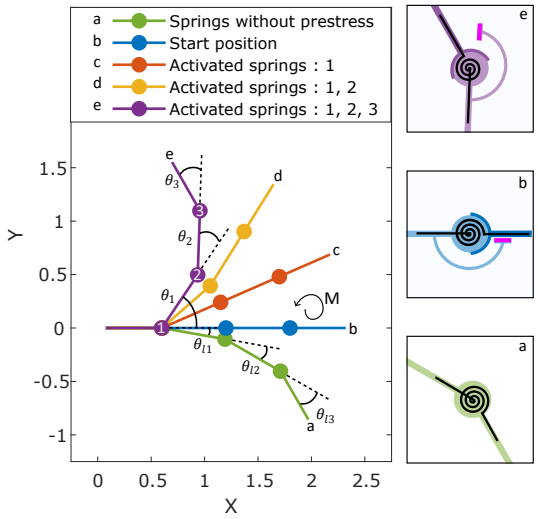

Fig. 2. Movement of system with three torsional springs initially prestressed and blocked horizontally. The circles correspond to torsional springs, and the lines correspond to rigid parts connecting the torsional springs. The three figures at the right represent the contact release of the third spring where the pink part is a mechanical stop.

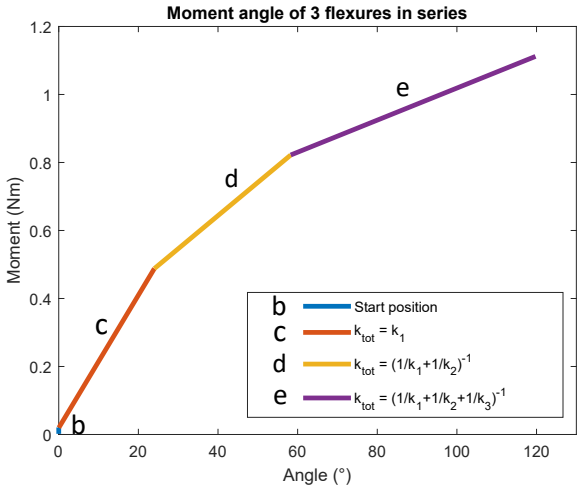

Fig. 3. Moment-angle of 3 springs in series, colors of the graph correspond to the configuration of the mechanism in Fig. 2 with the same color and letter.

1) Moment-angle characteristic: The paper aims to achieve a softening behavior in the proposed concept, and to assess this, simulations of the moment-angle characteristics are conducted. The input parameters for the PRBM include the initial prestress angles (in degrees), the stiffness of each spring, and the input moment. It is important to note that the relationship between moment and angle is assumed to be linear. The prestressed angle and stiffness determine the moment limits for each spring. This means that if the input moment is below the limit moment of a spring, that particular spring will not release its contact from the mechanical stop and will remain inactive. The limit moment for each spring is calculated as follows: $M_{li} = k_i \theta_{li}$, where $i = 1, .., N$ and N represents the number of springs. Once an input moment M is applied to the PRBM, the angle of each spring is determined using the following equations:

$$if M < M_{li}, \;\; then \;\; \theta_i = 0$$
$$if M > M_{li}, \;\; then \;\; \theta_i = \frac{M - M_{li}}{k_i}$$

The sum of these angles represents the global angle of the entire system. Finally, a moment-angle graph is generated to visualize the behavior, covering angles up to 120°.

2) Movement nodes: An animation is created to gain insight into the side-view movement of the concept before proceeding with the prototype construction. This animation represents the movement of the springs in relation to each other and is generated using transformation matrices. Fig. 4 shows the figure used to calculate the position of each node, labeled as n_1 to n_6. The global reference system, denoted as X and Y, is established, along with local reference systems. The

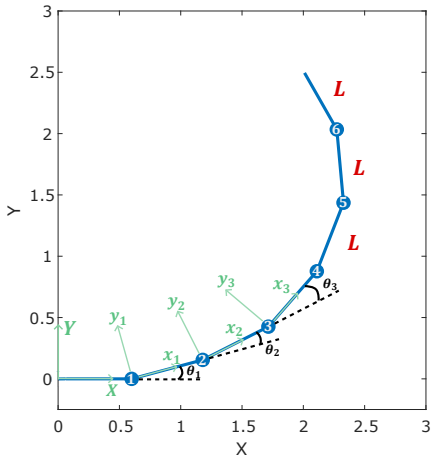

Fig. 4. Positions of springs. L is the distance between each spring, x_i and y_i are the local reference axes. X and Y are the global reference axes.

first local reference system is obtained by rotating the global reference system by an angle θ_1 around the Z-axis, resulting in the x_1 and y_1 axes. Subsequent local reference systems are created by rotating the x_1 and y_1 axes by an angle θ_2, and this process is repeated for the remaining local reference systems. Six torsional springs require five local reference systems. Assumptions are made that the system is fixed at the origin (0,0), and a counterclockwise moment is applied at the other end of the system. Additionally, the lengths between all torsional springs are assumed to be equal and represented by L. This assumption is solely for clarity in computations

and can be variable. The position of each node at any given moment can be determined using the following equations:

$$\vec{n}_1 = LX$$
$$\vec{n}_2 = Lcos(\theta_1)X + Lsin(\theta_1)Y + \vec{n}_1$$
$$\vec{n}_j = \sum_{j=3}^{N} (Lcos(\theta_{j-1})x_{j-2} + Lsin(\theta_{j-1})y_{j-2} + \vec{n}_{j-1})$$

A pattern can be observed starting from $\vec{n}_3$. This pattern can be expressed in matrix form for nodes n_3 and n_4, with the same principle applicable to springs above four. The equations can be transformed into the global reference system using transformation matrices:

$$\begin{bmatrix} x_1 \\ y_1 \end{bmatrix} = \begin{bmatrix} cos(\theta_1) & sin(\theta_1) \\ -sin(\theta_1) & cos(\theta_1) \end{bmatrix} \cdot \begin{bmatrix} X \\ Y \end{bmatrix} = T_1 \cdot \begin{bmatrix} X \\ Y \end{bmatrix}$$

$$\begin{bmatrix} x_2 \\ y_2 \end{bmatrix} = \begin{bmatrix} cos(\theta_2) & sin(\theta_2) \\ -sin(\theta_2) & cos(\theta_2) \end{bmatrix} \cdot \begin{bmatrix} x_1 \\ y_1 \end{bmatrix}$$

$$= \begin{bmatrix} cos(\theta_2) & sin(\theta_2) \\ -sin(\theta_2) & cos(\theta_2) \end{bmatrix} \cdot \begin{bmatrix} cos(\theta_1) & sin(\theta_1) \\ -sin(\theta_1) & cos(\theta_1) \end{bmatrix} \cdot \begin{bmatrix} X \\ Y \end{bmatrix}$$

$$= T_2 \cdot T_1 \cdot \begin{bmatrix} X \\ Y \end{bmatrix}$$

The transformation matrices (T_1 and T_2) convert the positions from one reference system to another, specifically from (x_1, y_1) to (X, Y) and from (x_2, y_2) to (x_1, y_1) respectively. Similar transformation matrices can be derived for the remaining local reference systems. For example, the transformation matrix for the fourth local reference system is as follows:

$$\begin{bmatrix} x_4 \\ y_4 \end{bmatrix} = T_4 \cdot T_3 \cdot T_2 \cdot T_1 \cdot \begin{bmatrix} X \\ Y \end{bmatrix}$$

By incorporating these equations with the transformation matrices into the position equations for each node, the positions can be calculated in the global reference system. Only the final equation for the sixth node is presented, but all other nodes follow a similar calculation method:

$$\begin{bmatrix} n_{6,X} \\ n_{6,Y} \end{bmatrix} = \begin{bmatrix} Lcos(\theta_5) \\ Lsin(\theta_5) \end{bmatrix}^T \cdot T_4 \cdot T_3 \cdot T_2 \cdot T_1 \cdot \begin{bmatrix} X \\ Y \end{bmatrix} + \begin{bmatrix} n_{5,X} \\ n_{5,Y} \end{bmatrix}$$

These equations, along with the transformation matrices, are implemented in code to generate an animation that visualizes the movement of the entire system from its initial position to its final position.

3) Optimization parameters: The optimization of the torsional bars' stiffness and prestresses aims to achieve an optimized moment-angle graph that aligns with the desired performance criteria. The optimization process involves selecting the nine parameters, three for the stiffness of the torsional bars and six for their prestress angles. Six springs are chosen for the optimization. Among these six springs, the first and second, the third and fourth, and the fifth and sixth springs have identical stiffness. The reason behind these choices will be explained in Section II-D. Furthermore, the cross-section and material of the torsional bars, specifically an ABS I-beam, are selected. The least square error cost function is employed for the optimization, and the interior point method, which finds a local minimum, is used to minimize this cost function. To establish correspondence with the chosen concept, certain constraints are incorporated into the code:

$$k_1 > k_2 > k_3$$
$$M_{l1} < M_{l2} < M_{l3} < M_{l4} < M_{l5} < M_{l6}$$

These constraints imply that the stiffness of the first torsional bar is greater than that of the third torsional bar and even greater than that of the fifth torsional bar. The limit moments are the smallest for the first torsional bar and the highest for the last. Consequently, the first spring to be activated is the stiffest, while the last one is the softest. This arrangement enables significant softening. Activating the softest spring first would result in less pronounced softening, as a stiffer spring in series has a smaller impact on reducing the overall stiffness than a softer spring. Additionally, each parameter's upper and lower bounds ensure that all the torsional bars operate within their elastic deformation range when prestressed.

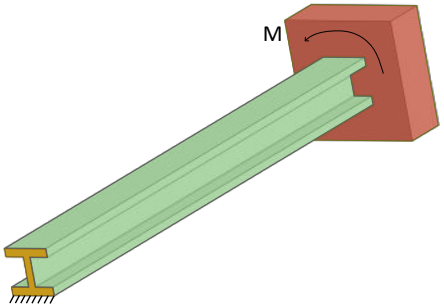

Fig. 5. Modeled I-beam for FEA, with a fixed support at the left side and an applied torque at the right side.

C. FEA

A FEA simulation was conducted to evaluate the stiffness and stress levels of an ABS I-beam represented as a solid structure. The simulation involved applying a uniform rotation to the entire cross-section on one side of the I-beam while fixing the other side, as illustrated in Fig. 5. The selection of an I-beam was motivated by its desirable characteristics, including linear torsional stiffness and high bending stiffness in both the x- and y-directions. A Poisson ratio of 0.3 and a linear isotropic elastic material model were utilized for the simulation. Due to the wide range of possible values for the Young's modulus of ABS [7, 8], experimental tests were conducted on a single I-beam, and the FEA results were adjusted to fit the experimental curve to determine the actual E-modulus

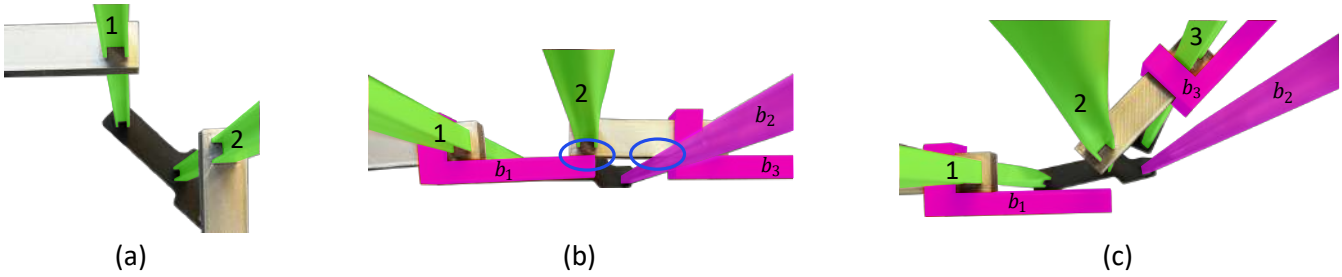

Fig. 6. Side view of concept with the pink's mechanical stops and the green torsional bars. (a) Relaxed torsional bars, no prestress. (b) Prestressed torsional bars, torsional bars stay in place because mechanical stops make contact, circled in blue. (c) End position, torsional bars are released from their mechanical stops.

of the I-beam. Furthermore, the FEA analysis allowed for the evaluation of stress levels in the I-beam, ensuring that the deformation caused by the applied rotation remained within the elastic deformation range. It should be noted that the I-beam profile used in this study was not optimized, leaving room for exploration of alternative profile options.

D. Prototype

The chosen design incorporates a symmetrical arrangement of torsional springs stacked on top of each other, as shown in Fig. 7. To simplify production, it is decided that all torsional beams have the same cross-section. This ensures that the only variable affecting the stiffness of a torsional beam is its length. In this design, consecutive pairs of springs, such as the first and second springs, the third and fourth springs, and the fifth and sixth springs, have the same length and stiffness. This design choice simplifies the attachment between the bars and reduces the system's overall weight.

For the sake of simplicity, a blue square is featured in Fig. 7, referred to as a "cell" for ease of explanation. Counting top-down, the orange square denotes the first row of the cell, while the red square represents the second row. When discussing the rigid bodies associated with a particular torsional bar, it refers to the rigid bodies situated directly below that specific torsional bar. Similarly, the rigid bodies connected to the preceding torsional bar are positioned above it.

The decision to employ six nodes was motivated by several factors. Firstly, an even number of springs was preferred to facilitate the design process. This is evident in the attachment of the rigid parts, where the rigid part attached to the second row lies in the middle, the gray part in Fig. 7. In contrast, the rigid parts attached to the first row are located at the torsional bar's endpoints. Secondly, employing a limited number of torsional bars offers the advantage of reducing the overall weight of the concept. However, this approach has a drawback of reduced softening effect and the potential for excessive stresses in the torsional bars. These high stresses may lead to elastic and plastic deformation when reaching the desired 120 degrees of rotation. On the other hand, more torsional bars would increase the weight and spatial requirements of the concept, which is undesirable for specific applications. It is worth noting that the prototype, with more springs, can achieve rotations exceeding 120 degrees, although this is not a requirement discussed in this paper. Thus, six nodes were selected as an optimal solution to strike a compromise between the prototype's weight and the a 120-degree rotation.

Following the optimization of the PRBM parameters, a prototype is developed. The length of each torsional beam is determined based on the stiffness values obtained from the PRBM optimization process. Additionally, the prestress angle for each torsional beam is derived from the PRBM. Subsequently, mechanical stops are designed to enable individual prestressing and mechanical blocking of each spring. Two types of mechanical stops are created: one for blocking the first row of each cell by directly contacting the next middle stop and another for blocking the second row of each cell, which requires an additional bar between the extremities of the second row to be blocked by the central part, as can be seen in Fig. 6. ABS I-beams are selected as was considered during the FEA analysis and optimization of the PRBM.

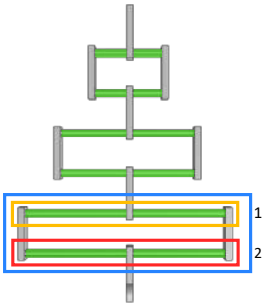

Fig. 7. Front view of CAD drawing of prototype, with green torsional bars. The blue square is a cell, the orange square is the first row of a cell and the red square is the second row of a cell.

E. Experimental validation

For the experimental validation, measurements were conducted on a single torsional bar to fit its stiffness to the FEA results. Additionally, measurements were taken on the entire prototype to compare its performance with the PRBM. An Althen®sensor capable of measuring both torque and angle was employed to test the torsional bar. The torsional bar was

fixed at one end and connected to the sensor at the other end, as depicted in Fig. 8. By applying a torsional input, the sensor recorded the torque required to rotate the torsional bar and the corresponding angle.

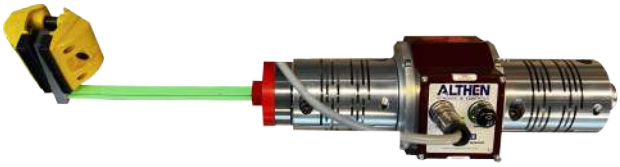

Fig. 8. Test setup of one torsional bar. The green part is the torsional bar, the yellow part on the left is the place where the torsional bar is fixed, and at the right side from the torsional bar is the sensor.

The same sensor used for testing a single torsional bar was employed for the complete prototype. However, due to each spring's sequential activation, the prototype's rotational center varied throughout its movement. Consequently, the sensor could not be placed on a stationary table, as was the case for testing a single torsional bar. Instead, the prototype was fixed on one side, and the other side was connected to the sensor using a bellow. This bellow was flexible in bending but rigid in torsion. Its purpose was to ensure that a pure moment was applied to the mechanism while minimizing the reaction forces. This required maintaining a straight line for the bellow. The sensor was allowed freedom of movement in the y- and z-directions. To achieve this, the sensor was mounted on a stool with wheels. To initiate the experiment, the stool was positioned at a height where the prototype was at its initial configuration, resulting in a total angle of 0°, and where the bellow remained straight. Torque was then applied to the prototype through the bellow. The stool was subsequently moved in the y- and z-directions to keep the bellow straight. This process was repeated for each torque application, covering the entire range of motion of the prototype (120°). The same procedure was repeated with the entire mechanism tested upside down. This was done to eliminate the influence of the prototype's mass on the measured torque. After completing the experiments, the data obtained was compared to the predictions of the PRBM. Additionally, the torsional moment-angle curve of the bellow was measured using the same method as for testing a single torsional bar. This measurement was necessary because the bellow could be considered as an additional spring in series with the entire system. By determining the stiffness of the bellow, a correction factor could be calculated to adjust the measured angle data. In the case of linear bellow stiffness, the correction factor (CF) was calculated as follows: $\theta_{new} = \theta_{old} - M_{measured} \times CF$, where CF represents the inverse of the bellow's stiffness in (°/Nm).

III. Results

The following sections will discuss the results of the FEA, PRBM, prototyping, and experimental validation.

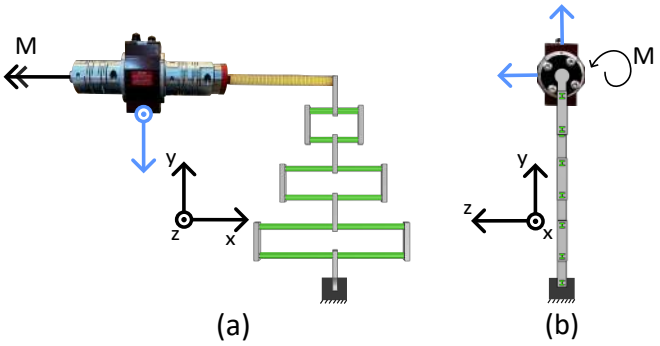

Fig. 9. Test setup of the whole prototype in the upward direction. The blue arrows are the degrees of freedom of the sensor, which are the y- and z-directions. The green parts are the torsional bars. (a) Front view. (b) Side view.

A. FEA

The FEA analysis confirmed the linear stiffness of the I-beam, as demonstrated in Section III-D. Fig. 10 depicts the stress levels obtained from the FEA simulation.

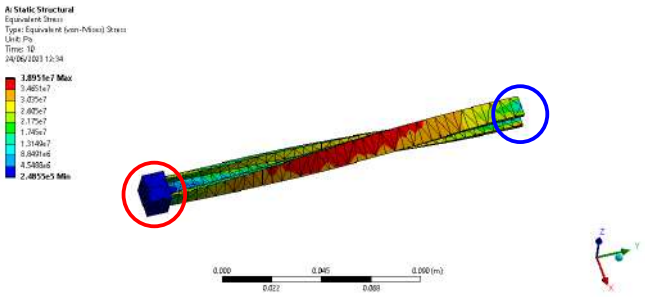

Fig. 10. Stress distribution of I-beam for a distributed applied moment. The blue circle represents the fixed endpoint of the I-beam, and the red circle represents the endpoint where the moment is applied.

B. PRBM

An optimization was conducted for nine parameters, including three different stiffness values and six different prestresses. As described in Section II-B, the first two torsional bars were assigned the same stiffness, followed by the third and fourth torsional bars with the same stiffness, and the fifth and sixth torsional bars with another equal stiffness. The optimization was performed using ABS I-beams with the cross-sectional dimensions from the prototype. The PRBM optimization focused on achieving three distinct softening curves, with the results presented in Fig. 11, Fig. 12, and Fig. 13.

C. Prototype

Following the FEA and PRBM simulations, a physical prototype was constructed, as illustrated in the front and side views in Fig. 14 and Fig. 15. In these figures, the torsional bars are green, while the mechanical stops are pink. As mentioned in Section II-B, counting top-down, the first two torsional bars share the same stiffness and length, followed

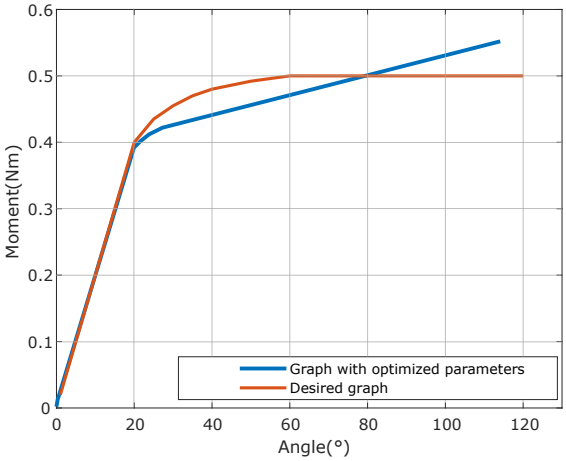

Fig. 11. Moment-angle graph of optimization of six torsional bars in series with different prestress and stiffness for a desired graph with a constant force behavior.

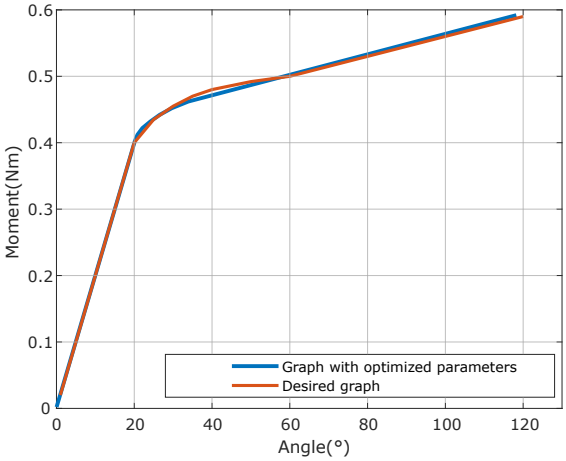

Fig. 12. Moment-angle graph of optimization of six torsional bars in series with different prestress and stiffness for a desired graph with rapid activation of each torsional bar.

by the next two torsional bars, which are softer than the first pair. The final torsional bars are the longest and exhibit the lowest stiffness within the entire system. The mechanical stops consist of two types: vertical parts located in the middle of the first, third, and fifth torsional bars, denoted as b_1, b_3, b_5, and metal parts attached to the extremities of the second, fourth, and sixth torsional bars, designated as b_2, b_4, b_6. These stops make contact with the vertical parts of the corresponding torsional bars themselves. Fig. 15 illustrates the side view of the prototype, and Fig. 6 shows a close-up of the working principle of the mechanical stops in configuration (a) as the unprestressed position, (b) as the initial position, and (c) as the end position. It is evident that in the initial position, all mechanical stops make contact, while in the end position, they are released.

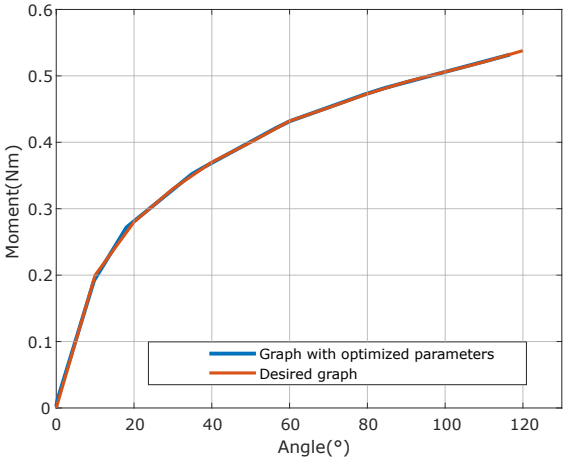

Fig. 13. Moment-angle graph of optimization of six torsional bars in series with different prestress and stiffness for a desired graph with gradual activation of each torsional bar.

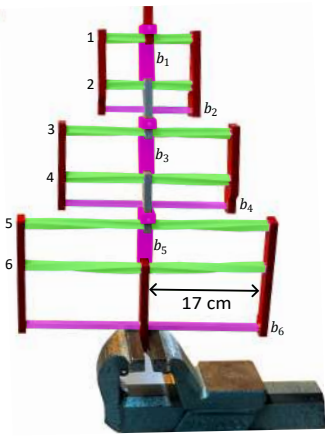

Fig. 14. Front view of the prototype in initial position: the green parts are the torsional bars, indicated by numbers and their corresponding mechanical stops in pink, indicated by b_i.

D. Experimental validation

Fig. 16 and Fig. 17 show the experimental validation of the torsional bar's stiffness. The experimental results confirm the FEA prediction of linear torsional stiffness for I-beams. Additionally, I-beams with lengths ranging from 5 cm to 20 cm were tested to assess their stiffness. The relationship between beam length and stiffness is inversely proportional, which follows the rule that if a flexure's length is doubled, its stiffness is halved.

For the complete prototype, the experimental setup is illustrated in Fig. 18 and Fig. 19. Once again, the pink colored parts represent the mechanical stops, the green parts represent the torsional bars, and the yellow part represents the bellow. The results for two different optimized curves are shown in Fig. 20 and Fig. 21.

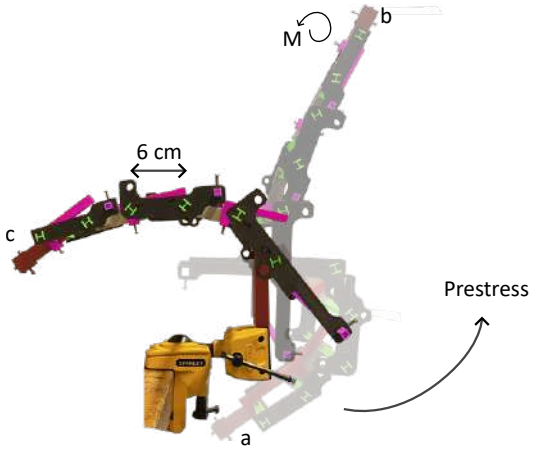

Fig. 15. Side view of the final prototype. The green parts are the torsional bars and the pink parts are the mechanical stops. (a) Configuration without prestress. (b) Initial configuration. (c) Final configuration.

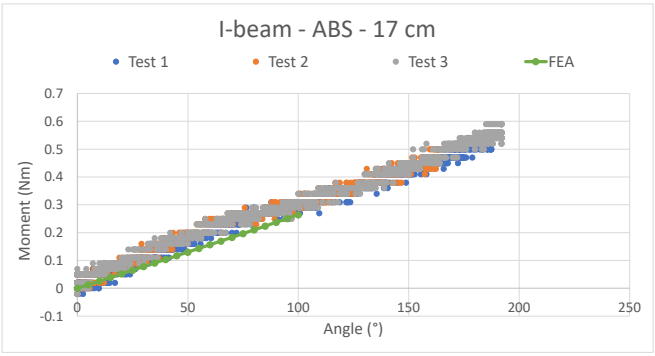

Fig. 16. Moment-angle graph of I beam in ABS, with dimensions: t_w = 0.0012m, t_f = 0.0016m, h = 0.0102m, w_I = 0.0100m, length = 0.170m.

IV. Discussion

For the experimental evaluation of a single 17 cm torsional bar, with one end fixed and the sensor positioned at the opposing side, the overall trend of the experimental results aligns with the simulated results. However, there is a variation in constraint between the experiments and the FEA. As illustrated in Fig. 10, the rotation is uniformly applied to the entire cross-section of the I-beam, preventing any changes in its form. In practice, the prototype allows for slight warping in the z-direction during rotation since the I-beams are not fully constrained, but rather restricted through an I-shaped hole.

To enhance the accuracy of future experimental results, it is advisable to consider the misalignment between the sensor and the I-beam. Moreover, the choice of E-modulus significantly affects the FEA outcomes. ABS has a wide range of potential E-modulus values, resulting in having to fit the moment-angle curve of the FEA with the experimental curves. As has been done in this paper, it is crucial to determine an E-modulus that aligns with the chosen material.

The experimental upward and upside-down tests closely followed the simulated PRBM. Taking the average results from

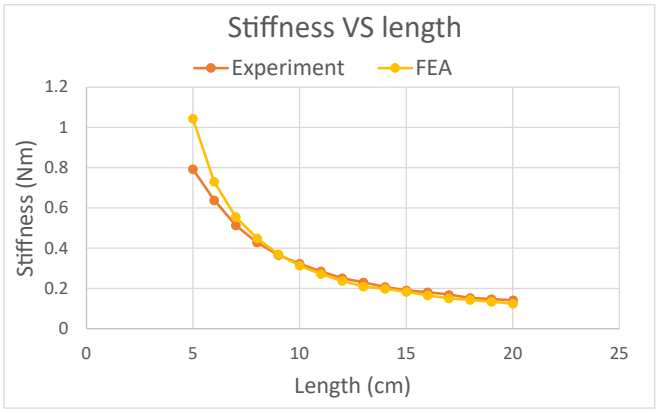

Fig. 17. Stiffness versus length of ABS I-beam.

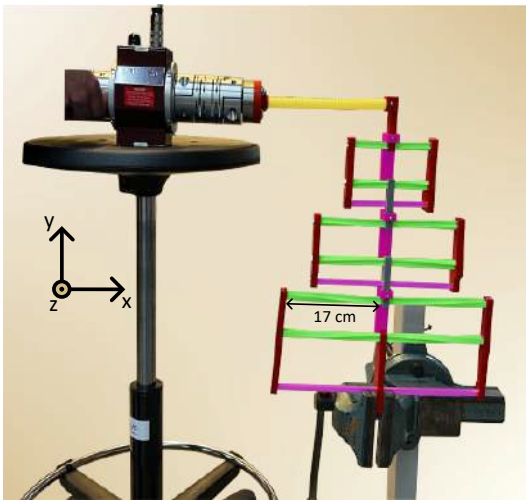

Fig. 18. Test setup of the whole prototype in the upward direction. The green parts are the torsional bars, the yellow part is the bellow and the pink parts are the mechanical stops.

both tests yields an alignment between the experimental and simulation graphs. Up to a rotation of 30°, both experiments follow a similar path. However, divergence occurs beyond this point. In the upside-down test, a higher torque is necessary to keep the bellow straight due to the need for torque to compensate for the prototype's mass. As the rotation angle exceeds 30°, the bellow progressively bears more of the prototype's mass, causing further deviation from the simulation. Similarly, gravity facilitates the prototype's alignment with the bellow in the upward test, requiring less torque to maintain bellow straightness. In further research, optimizing the design of rigid bodies between the torsional springs and considering lighter alternatives to the horizontal stops for springs 2, 4, and 6 are recommended to reduce prototype mass.

The primary challenge during the testing process is the changing global rotational center caused by the sequential activation of torsional bars. Consequently, the prototype lacks a known defined end-point path. Furthermore, the desire to measure a pure moment introduces additional complexities

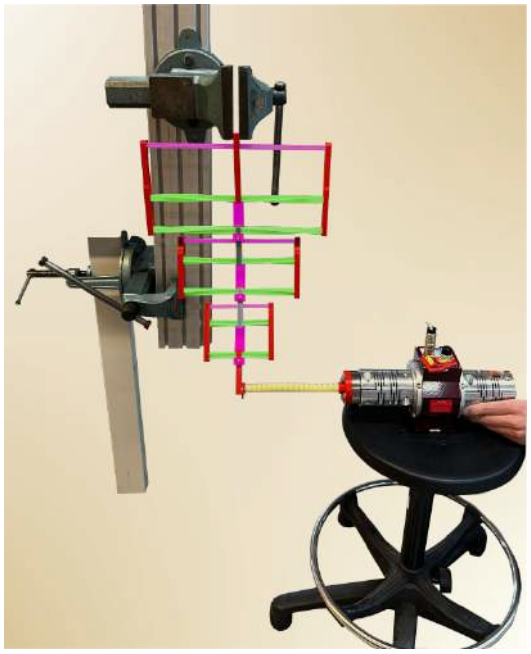

Fig. 19. Test setup of the whole prototype in the upside down direction. The green parts are the torsional bars, the yellow part is the bellow and the pink parts are the mechanical stops.

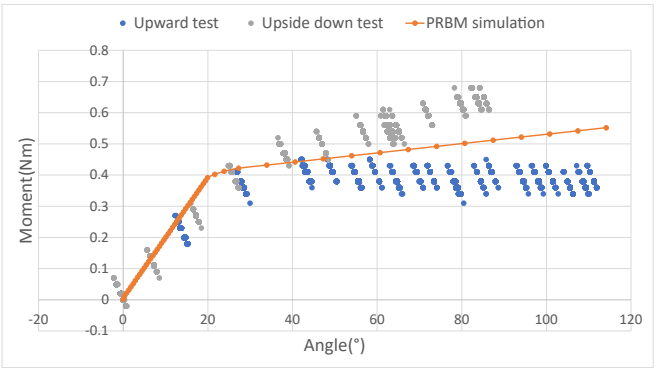

Fig. 20. Moment-angle graph of the complete prototype with rapid activation of each torsional bar.

to the testing process, necessitating the avoidance of reaction forces. To address these issues, the sensor was allowed freedom in the y- and z-directions, and a bellow was introduced between the sensor and the prototype to minimize reaction forces. However, the bellow, acting as an additional torsional spring in series, affected the test results, and a correction factor needed to be calculated. Additionally, testing the prototype upside down presented limitations, preventing it from reaching the end position due to excessive prototype mass, rendering bellow straightness unachievable. The bellow's straightness was controlled visually, which is a suboptimal method to control the straightness of the bellow.

Furthermore, the observed test results exhibit a distinct pattern of diagonal lines. Initially, these lines appeared vertical, attributed to the sensor's high angle accuracy but relatively

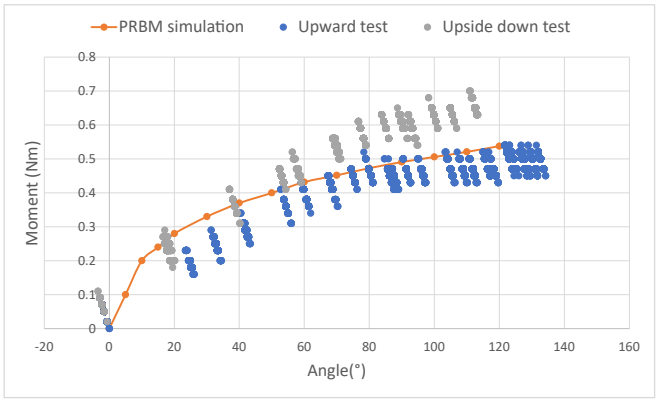

Fig. 21. Moment-angle graph of the complete prototype, with gradual activation of each torsional bar.

lower torque accuracy. However, the vertical lines transformed into diagonal lines due to the inclusion of a correction factor to account for the impact of the bellow. Notably, the diagonal pattern consistently comprises a series of individual data points separated by a specific spacing. This pattern arises from conducting the tests utilizing the digital output of the sensor, which presents values with a resolution of 0.01Nm. Additionally, the signal-to-noise ratio is high, especially since the signal is at the lower end of the range of measurement of the sensor. The sensor in this study has a wide measurement range of 0.01Nm- 225Nm, while the experimental setup only requires a maximum moment of 0.7Nm.

During the experiments, the I-beams experienced loading not only in torsion but also in bending. The effect of bending is still unknown, but could be looked into for future research. Several approaches can mitigate this bending effect. Firstly, adding additional straight beams, not loaded, in parallel, can reduce bending's influence. Alternatively, replacing the I-beams with profiles with uniformly higher bending stiffness in all directions while maintaining low torsional stiffness could be considered. It is important to note that altering the profile may introduce non-linear stiffness, necessitating the implementation of this non-linearity in the PRBM code. Accepting that the I-beam exhibits finite bending stiffness and incorporating bending behavior into the PRBM simulation is another viable option. Additionally, incorporating the mass's effect on experimental results in the PRBM simulation or horizontally testing the prototype (which may be challenging given the sensor choice) can be explored. The length of the bellow has not been thoroughly investigated. Longer bellows contribute to lower bending stiffness, thereby improving torque and angle accuracy measurements. If the bellow is excessively long, it will be more prone to bending under the weight of the prototype, leading to the inability to maintain its straight configuration. However, to have better torque accuracy, the sensor should be changed.

In general, the results demonstrate that the physical prototype aligns with the trend observed in the simulated moment-angle curve. Although slight variations in slope exist between

the simulated curve and experimental findings, the overall trend remains consistent.

In future research, it is recommended to investigate alternative cross-sections to determine the optimal choice. The ideal cross-section should exhibit low torsional stiffness compared to bending stiffness, while maximizing torsional stiffness for the chosen material. Additionally, the new profile should either maintain a linear moment-angle characteristic or demonstrate a desirable softening behavior. It is important to avoid profiles with a stiffening behavior, as the overall objective is to achieve a softening global stiffness. Incorporating non-linear torsional stiffness in the optimization if a different cross-section exhibits such behavior is worth investigating. Furthermore, the current interior-point optimization approach yields a local minimum. Changing this algorithm to, for example, a multistart solver or a genetic algorithm would reduce the influence of the initial guess. Additionally, conducting FEA on the entire prototype, rather than a single beam, would provide valuable insights. It could be focused on increasing the moment's capability to advance the project. The prototype utilizing ABS material currently allows for a maximum moment of only 0.5-0.6Nm. Switching from ABS to materials like spring steel could significantly enhance the moment capacity. An alternative design approach that should be explored involves investigating the implementation of varying stiffness in each compliant beam, rather than using identical stiffness for every beam pair. Additionally, considering the development of a monolithic compliant mechanism, without incorporating rigid bodies within the prototype, could be explored if it does not significantly complicate the manufacturing process. One potential application for this study is the development of a back-support system for exoskeletons. However, it is essential to increase the moment-support capability to enable its practical use.

V. Conclusion

In summary, this study has successfully demonstrated a unique approach to achieve a softening moment-angle graph response by utilizing compliant parts. By using the principle of contact release, the design incorporates initially prestressed torsional bars arranged in series, with rigid bodies separating them. This arrangement allows for the gradual activation of the springs, resulting in a desirable softening behavior.

A PRBM was developed to calculate the moment-angle behavior of the complete prototype. The PRBM optimization process involved adjusting the stiffness of the torsional bars and their initial prestress, guided by a cost function that minimized the difference between the desired and calculated graphs. Additionally, a FEA was employed to analyze the torsional bars' mechanical behavior, providing valuable insights into their individual response.

Experimental validation was conducted using a constructed prototype designed based on the optimized parameters obtained from the PRBM. The experimental results closely aligned with the predicted curves from the FEA and PRBM, showcasing the effectiveness of the proposed approach. Future investigations could explore different cross-sections, materials, and optimization techniques to further enhance performance and expand the application scope of this concept.

References

[1] L. L. Howell, "Compliant mechanisms," in *21st Century Kinematics*, J. M. McCarthy, Ed. London: Springer London, 2013, pp. 189–216.

[2] J. Fader, "Torsion bar with multiple arm adjusters for a vehicle suspension system," Patent, US6425594B1, 2002. [Online]. Available: https://patents.google.com/patent/US6425594B1/en

[3] E. J. Eshelman, "Multi-rate torsion bar independent suspension spring," Patent, US6945522B2, 2005. [Online]. Available: https://patents.google.com/patent/US6945522B2/en

[4] S. van Nes, "The use of a rigid linkage balancer with torsion springs to realize nonlinear moment-angle characteristics," Master's thesis, Delft University of Technology, 2022. [Online]. Available: http://resolver.tudelft.nl/uuid:71f96a22-584c-4b6d-9708-7c781810794b

[5] M. R. Claus, "Gravity balancing using configurations of torsion bars; with application to the hci foldable container," Master's thesis, Delft University of Technology, 2008.

[6] G. Radaelli, "Synthesis of mechanisms with prescribed elastic load-displacement characteristics," Ph.D. dissertation, Delft University of Technology, 2017.

[7] A. K. H. C. Fatima Sabah, Achraf Wahid and M. EL-ghorba, "Failure analysis of acrylonitrile butadiene styrene (abs) materials and damage modeling by fracture," *International Journal of Performability Engineering*, vol. 15, no. 9, p. 2285, 2019.

[8] E. Peters, *Plastics: Thermoplastics, Thermosets, and Elastomers*, 11 2007, pp. 335 – 355.

4

Discussion

4.1. Discussion research paper

The experimental testing of a single torsional bar with one end fixed and a sensor at the opposite side yielded results that matched the simulations. Moreover, the experimental tests for the complete prototype, conducted in an upward and upside-down orientation together, closely followed the simulated PRBM. However, individual divergence occurred beyond a 30° rotation angle due to the prototype's mass. Optimizing the design of rigid bodies between torsional springs and considering lighter alternatives for horizontal stops is recommended to reduce prototype mass.

During testing, the changing location of the global rotational center and the desire to measure a pure moment posed challenges, requiring the avoidance of reaction forces. Introducing a bellow and the freedom of the sensor in the y- and z-directions addressed these challenges. However, the presence of the bellow affected the test results as it acted as an additional spring in series with the entire concept, necessitating a correction factor.

Future research can explore the bending effect on the I-beams, consider alternative cross-sections, optimize the optimization algorithm, conduct FEA on the entire prototype, increase the moment capacity, and explore varying stiffness in compliant beams. A potential application is the development of a back-support system for exoskeletons, which would require increased moment-support capability.

4.2. Discussion implementation for exoskeleton

This concept exhibits favorable characteristics for application in an exoskeleton, including a softening behavior and distributed stress levels across the compliant components. Moreover, it requires fewer parts compared to the Laevo smart joints and has the potential to be lighter if appropriate materials are used. However, the current prototype does not deliver the required support for an exoskeleton, being 50 times too low. To address this limitation, the material and cross-section of the torsional beams can be modified. The current exoskeleton has a total weight of around 4kg, with the smart joints accounting for 1.24kg, equivalent to 30% of the overall weight. So, it is desirable for the new concept to weigh less than the smart joints. By using spring steel instead of ABS for the I-beams, the support can exceed 20Nm, as outlined in the calculations in Appendix A. Additionally, the concept's weight with spring steel is approximately 1.2kg, showing promise for practical implementation in an exoskeleton. However, it is important to note that the yield stress considered in the analysis is specifically for a strip, and it cannot be assumed that an I-profile would have the same yield stress. In practice, the yield stress of an I-profile might be lower than that of a strip. Therefore, it is essential to consider the specific material properties and dimensions of the chosen I-beam profile to accurately determine its yield stress and ensure its suitability for the prototype.

Furthermore, it is crucial to incorporate spine extension in the compliant spine design, considering the offset from the hip joint. Neglecting this factor could result in discomforting reaction forces exerted on the wearer, especially at the attachment points of the exoskeleton, such as the shoulders. So this extension is mainly important for the wearer's comfort. Integrating Houweling's spine concept in conjunction with the current design would be beneficial to address this requirement [5]. Houweling's spine, which focuses on creating a compliant spine with lower axial stiffness than bending stiffness,

could provide the extension capability for the exoskeleton. Combining the two concepts could allow the exoskeleton to achieve the desired range of motion while extending.

Moreover, the attachment points of the concept to the exoskeleton should be carefully considered to avoid hindering the user's movements. Rigid connections at the top and bottom of the concept should be avoided.

Another limitation of this concept is its inability to offer constant or negative stiffness. Attaining zero stiffness would necessitate an infinite amount of prestressing in a zero-stiffness spring. Although the moment-angle curve can be adjusted to a certain degree, the overall softening behavior heavily relies on the softest spring within the system. As the length of a beam increases, its stiffness decreases, but this is constrained by the spatial limitations inherent in exoskeleton applications. Therefore, finding an optimal balance between stiffness and spatial constraints is crucial when implementing this concept in practical exoskeleton designs.

Additionally, it is important to consider the creep or relaxation of the material over time, as the torsional beams are always prestressed. This phenomenon could potentially impact the performance and behavior of the concept, and further investigation into the long-term effects of creep and relaxation is recommended to ensure the system's reliability.

Further research should focus on optimizing the shape of the concept during bending to closely conform to the body without impeding movements. This can be achieved by adjusting the lengths between the torsional bars or rearranging the order of torsional bars with different stiffnesses, ensuring that the first torsional bar to rotate is not at an endpoint.

The current implementation of the concept focuses solely on pure moment loading. However, when the concept is attached to the human body within an exoskeleton, it will be subjected to various movements and forces that are not pure moment loading. Further research and investigation could be conducted in this area to understand how these additional forces impact the effectiveness and functionality of the concept. By exploring and analyzing the influence of different movements and forces on the concept, potential limitations or areas for improvement can be identified, leading to a more comprehensive and robust design.

5

Conclusion

In conclusion, the research paper in chapter 3 presents a compliant concept with a softening behavior using the contact-release principle. A prototype was built to test if the contact release would work. The main challenge was testing the prototype, as the desire was to measure a pure moment. This was solved by introducing a bellow and granting freedom to the sensor in the y- and z-directions. While the bellow affected the test results and required a correction factor, the experimental testing demonstrated a close match between the prototype and the simulations.

In conclusion, the concept presented in this paper exhibits promising potential for exoskeleton applications, particularly due to its softening behavior and the advantage of requiring fewer parts compared to conventional exoskeleton components, such as the Laevo smart joints. To meet the support requirements, modifications to the material and cross-section of the torsional beams are necessary. Incorporating spine extension and optimizing the concept's shape during bending are crucial for improving functionality. Attention should be paid to the attachment points and the limitations of achieving constant stiffness. Future research should address these challenges and explore alternative designs to enhance the concept's performance and optimize the shape during bending to align closely with the body's contours without restricting the movements.

References

[1] URL: https://creator.nightcafe.studio/creation/3TgGLXOsf6TynVFvdm5L.

[2] URL: https://www.laevo-exoskeletons.com/spine-compression-basics.

[3] URL: https://www.laevo-exoskeletons.com/.

[4] Tim Bosch et al. “The effects of a passive exoskeleton on muscle activity, discomfort and endurance time in forward bending work”. In: *Applied Ergonomics* 54 (2016), pp. 212–217. ISSN: 0003-6870. DOI: https://doi.org/10.1016/j.apergo.2015.12.003. URL: https://www.sciencedirect.com/science/article/pii/S0003687015301241.

[5] Stijn Houweling. “Slender compliant mechanism with a low axial-bending stiffness ratio for use in an exoskeleton”. English. MA thesis. Delft University of Technology, 2022. URL: http://resolver.tudelft.nl/uuid:72083693-654b-4e61-8d76-cca432a4d622.

[6] Larry L. Howell. “Compliant Mechanisms”. In: *21st Century Kinematics*. Ed. by J. Michael McCarthy. London: Springer London, 2013, pp. 189–216. ISBN: 978-1-4471-4510-3.

[7] G. Radaelli and J.L. Herder. “Gravity balanced compliant shell mechanisms”. In: *International Journal of Solids and Structures* 118-119 (2017), pp. 78–88. ISSN: 0020-7683. DOI: https://doi.org/10.1016/j.ijsolstr.2017.04.021. URL: https://www.sciencedirect.com/science/article/pii/S0020768317301737.

A

Calculations for exoskeleton

Preliminary calculations were performed to assess the feasibility of implementing this concept in a supportive exoskeleton. High-strength spring steel I-beams were chosen for the simulations. The material properties of the high-strength spring steel, such as density, Poisson's ratio, and Young's modulus, were incorporated into the FEA to obtain moment-angle graphs and beam stresses. The Poisson's ratio and Young's modulus of the high-strength spring steel were determined to be 0.29 and 190GPa, respectively. The selected spring steel yield stress is 1.120GPa, as indicated in the certificate provided in Appendix F. Considering that the dimensions of the I-profile used in the study resulted in stresses exceeding the yield stress, slight adjustments were made to the parameters. The revised dimensions for the beam, measuring 170mm in length and intended for a 60° rotation, are as follows: $w_I = 0.013m$, $h = 0.013m$, $t_f = 0.0008m$, and $t_w = 0.001m$. These modifications ensure that the beam remains below the yield stress. As the prototype comprises six beams in series and a total range of motion of 120° is desired, the 170mm beam can be prestressed up to 40°, allowing for a 20° rotation. In contrast, a beam three times shorter would be capable of a 20° rotation without any prestress.

The stress distribution on the beam, shown in Fig. A.1, indicates that peak stresses occur at the attachment points, while the overall stress is 0.61 GPa, which is below the yield stress. However, stress levels at the attachment points exceed the yield stress. Optimizing the design is believed to reduce the stress levels at these points to an acceptable level. The stiffness values for beams of 5.5cm, 11cm, and 17cm were obtained from the FEA and found to be 36.25Nm/rad, 18.13Nm/rad, and 11.73 Nm/rad, respectively. In Fig.A.3 the moment-angle graph of a 170mm I-beam in spring steel can be found.

Subsequently, the stiffness values for different beam lengths were incorporated into the PRBM simulation of the moment-angle graph for the entire concept. Prestress angles of [0°, 2°, 15°, 20°, 35°, 40°] were chosen, ranging from the stiffest to the softest spring. The resulting total moment-angle graph is shown in Fig. A.3.

Additionally, the mass of the torsional beams was calculated using the known density and the volume formula: $V_1 = w_I \cdot 2 \cdot t_f \cdot length + t_w \cdot (h - 2 \cdot tf) \cdot length$, where V_1 represents the volume of the first torsional bar. Considering that there are four torsional bars in a cell, as explained in the research paper, the total mass of all the torsional bars can be calculated as $V_{\text{tot}} = 4 \cdot (V_1 + V_2 + V_3)$. Finally, the mass is determined as $m = V_{\text{tot}} \cdot \rho$, with $V_{\text{tot}} = 7.310 \times 10^{-6}\text{m}^3$, and $\rho = 7850\text{kg/m}^3$, resulting in approximately 0.350kg. The measured mass of the ABS prototype was approximately 0.300kg for the complete prototype and 0.090kg for the torsional bars, yielding a ratio of 3.33. Scaling the complete profile using the same principle would result in a weight of 0.350kg$\times$ 3.33 = 1.17kg. However, optimizing the design of the rigid parts to minimize mass could potentially reduce this weight. Notably, the combined weight of two smart joints is 1.240kg, similar to the estimated mass.

This estimation provides an initial insight into the feasibility of the concept, but additional work is required to optimize the I-profile or explore alternative cross-sections. It is important to prioritize a high bending stiffness and low torsional stiffness when considering potential design modifications.

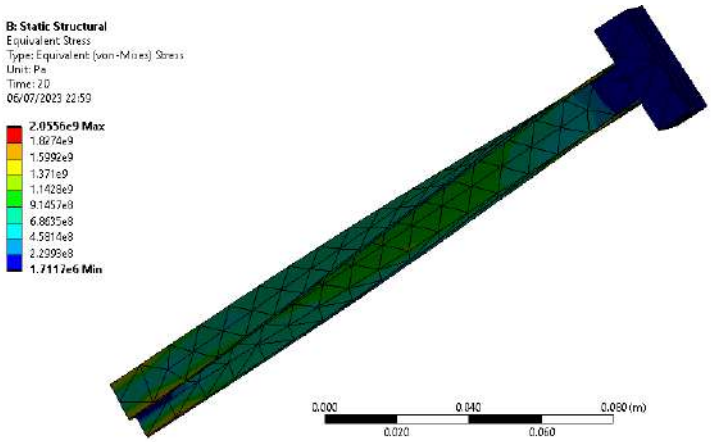

(a) Stress levels of the whole beam.

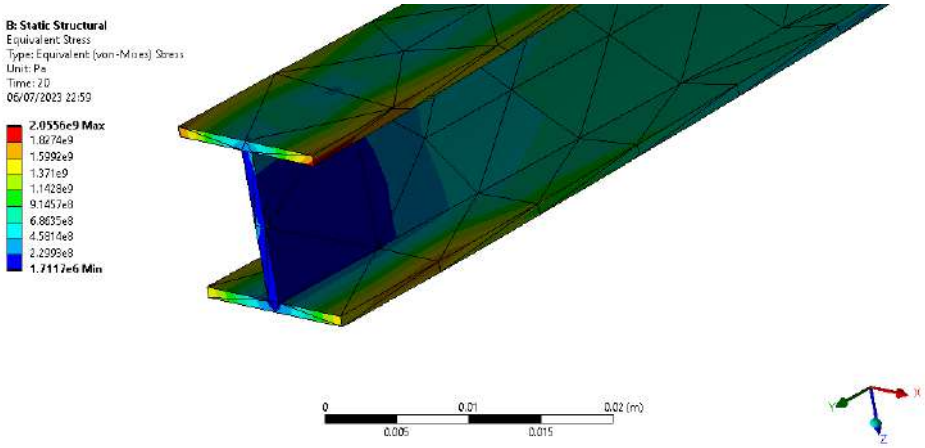

(b) Stress levels at the attachment point.

Figure A.1: Stresses of I-beam in spring steel with a rotation of 60° with the parameters: t_w = 0.001m, t_f = 0.0008m, h = 0.013m, w_I = 0.013m, length = 0.170m.

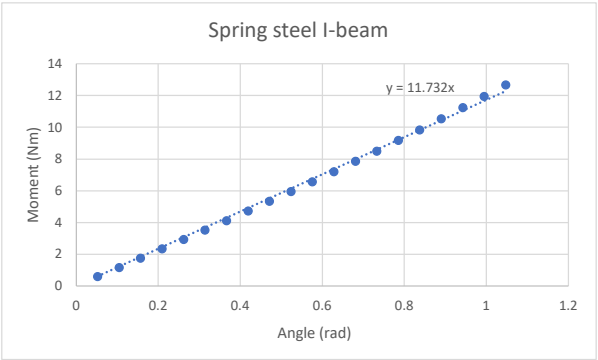

Figure A.2: Moment-angle of I-beam in springsteel: t_w = 0.001m, t_f = 0.0008m, h = 0.013m, w_I = 0.013m, length = 0.170m.

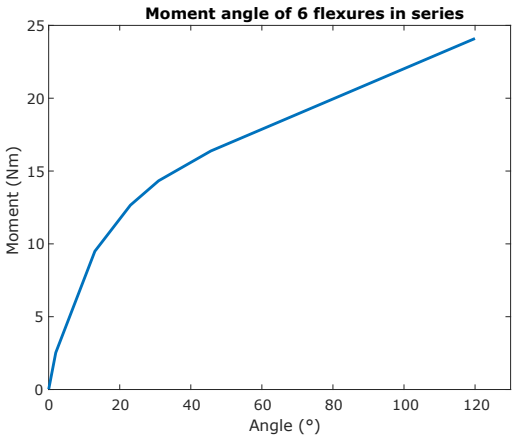

Figure A.3: Moment-angle of compliant spine in spring steel: t_w = 0.001m, t_f = 0.0008m, h = 0.013m, w_I = 0.013m, length = 0.170m. Prestress angles in degrees: [0,2,15,20,35,40] from stiffest spring to softest spring.

B

Concept generation

This section will discuss two concepts for creating a compliant spine that provides non-linear lower back support. The Laevo FLEX exoskeleton currently has a non-linear moment-angle behavior, allowing for significant angular displacement and providing maximum support of 40Nm or 20Nm (for medium and ultra-light size gas springs, respectively). A set of requirements for the compliant spine has been established, including compliance, non-linear behavior, large rotation capability, and a minimum support of 20Nm. Initially, the spine was intended to be extendable due to its offset position from the human spine. However, to simplify the design and reduce complexity, the extendability requirement was removed. Instead, concepts were developed with the understanding that an extendable part could be added in series, such as Houweling's extendable spine concept [5].

B.1. Concept 1

The first concept is inspired by the principle of a tape spring, where the tape spring remains straight under a certain load until a force threshold is exceeded, causing buckling and softening behavior, see Figure B.1. The idea is to position a large curved sheet on the individual's back, as shown in Figure B.2a. By utilizing shape optimization, the desired non-linear moment-angle response can be achieved while closely conforming to the body and allowing unrestricted movement.

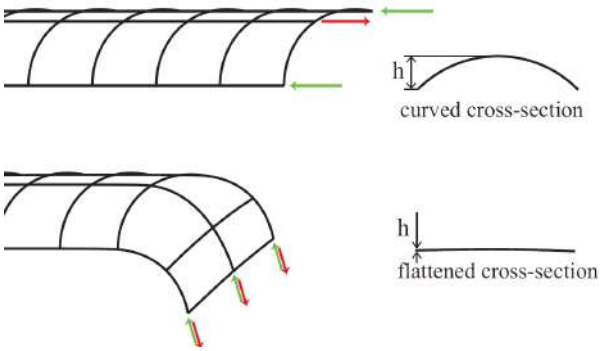

Figure B.1: Tape spring with a curved profile on top and the tape spring with a flat profile when buckling on bottom [7].

B.2. Concept 2

The second concept utilizes the concept of contact release, as explained in chapter 3. Multiple torsional bars are arranged in series, with each bar prestressed and maintained in a prestressed state by a contact point. When the contact is released, the torsional bar is activated and undergoes movement. The concept displays a softening moment-angle response by activating more springs in series. The concept is illustrated in Figure B.2b, where the horizontal bars represent torsional springs and the vertical bars represent the contact points between the torsional springs in series.

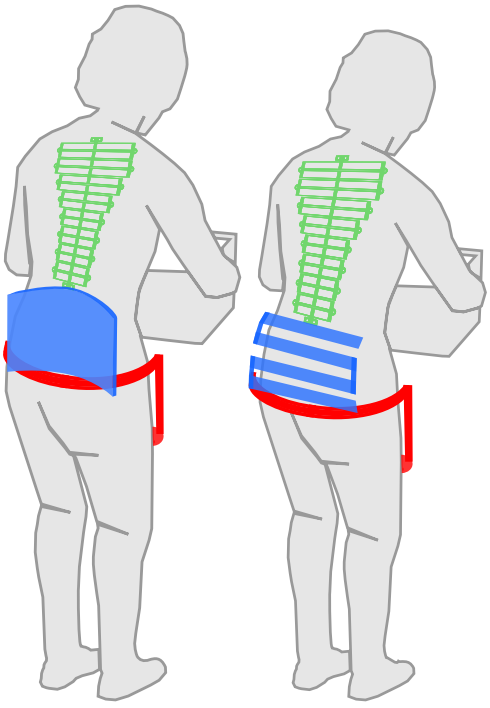

(a) Concept 1: blue part is a curved sheet.

(b) Concept 2: blue parts are the torsional springs in series.

Figure B.2: Concept solutions, with the blue part being the concept, the red is a hipframe, and the grey part is Houweling's extendable spine [5].

B.3. Comparison concepts

The first concept offers the advantages of simplicity and the ability to tune non-linearity and shape through shape optimization. However, there are concerns regarding concentrated stress at the buckling location and potentially limited support capability. Additionally, the deformed shape is directly linked to the moment-angle characteristic. On the other hand, the second concept distributes the load, resulting in stress distribution across all torsional bars. Support can be increased by adding springs in parallel, and the range of motion can be expanded by incorporating more torsional bars in series. However, this concept requires additional stops contributing to the weight of the mechanism, and not all material is utilized for energy storage.

Considering these factors, the second concept was chosen due to the ability to decouple the moment-angle characteristic from the deformed shape and the potential for higher support by incorporating springs in parallel and a larger range of motion by adding torsional bars in series.

C

Prototyping

Once the chosen concept was selected, a first prototype of the compliant spine was developed. The initial prototype used a cruciform cross-section, providing stiffness in the bending direction and flexibility in the torsional direction. The design consisted of three torsional beams connected in series, each connected to the other through a rigid body. A tower-like structure was incorporated to enable the contact release mechanism (see Figure C.2). One end of the tower was fixed to the rigid body with an attachment based on a gear-like form, while the other end remained free. The tower made contact with the cruciform beam, acting as the mechanical stop for the prestressed beam. The components of the prototype were fabricated using PLA material through 3D printing and can be seen in Figure C.1.

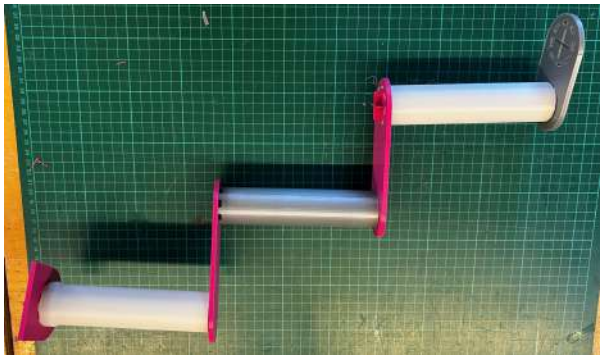

Figure C.1: First prototype of three torsional bars in series.

Although the initial prototype achieved the desired functionality, certain adjustments were necessary for further improvement. Initially, the torsional bars could not be stacked vertically due to incorrect placement of contact points for the middle torsional bar. This led to a zigzag prototype. To address this issue, the contact point of the middle tower needed to be mirrored, allowing for proper alignment of the torsional bars. Additionally, the original design required complete disassembly to release the prestress of the torsional bars. To simplify this process, the towers were printed in two parts, allowing them to slide along each other in the rotational direction. Bolts were introduced to maintain the prestress and prevent unintended sliding. Removing the bolts released the prestress, eliminating the need for complete disassembly. These modifications enhanced the functionality of the prototype, as depicted in Figure C.2 and Figure C.3. The light blue parts in Figure C.3 are additional printed parts that achieve the parallel alignment of the torsional bars. The rotation of 120° was successfully achieved with four torsional cruciform bars arranged in series.

Despite the success in achieving the desired rotation, the initial prototype had some limitations. The design involved multiple components and the addition and removal of prestress increased its complexity and weight. Consequently, the prototype faced challenges when placed in a vertical position due to its own weight. To address issues related to the torsional bars needing to be parallel to each other, a

(a) Top view towers, with X-beam - mirrored.

(b) Side view.

Figure C.2: Towers.

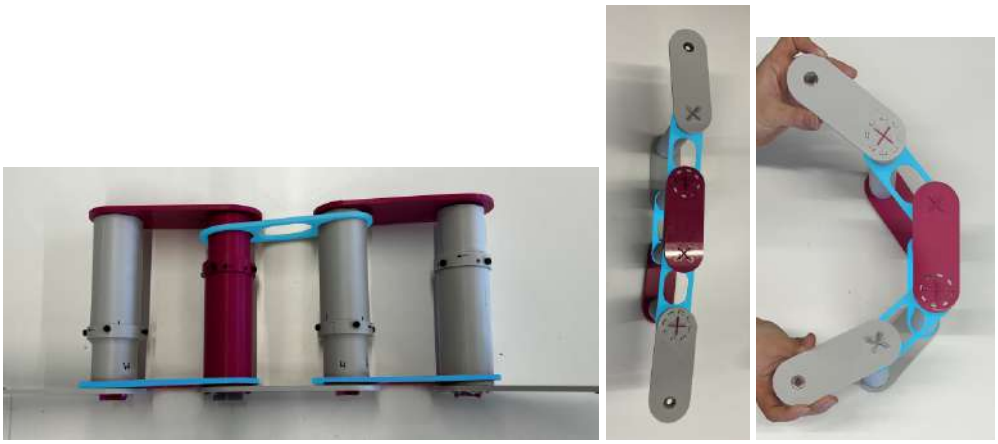

(a) Front view.

(b) Top view in the start position.

(c) Top view in the end position.

Figure C.3: Second prototype, blue parts are necessary to keep towers parallel to each other.

symmetrical design was implemented as an improvement over the original zigzag design. Moreover, the towers were eliminated, necessitating the development of alternative mechanical stops.

Next, a new design based on contact release was constructed, replacing the cruciform beams with I-beams with linear torsional stiffness. The prestress and length of the torsional bars were determined through PRBM optimization. The final design of the compliant spine, shown in Figure C.4, featured mechanical stops in pink and torsional bars in green. The principles of the mechanical stops are explained in chapter 3. The I-beam was constructed using ABS material, while the rigid parts were 3D printed using ABS as well. The significant leap in design iteration resulted from a prolonged brainstorming process. Through continuous exploration and discussion, new ideas and insights emerged, eventually leading to the development of the current and final prototype.

(a) Front view. **(b)** Side view.

Figure C.4: Last prototype, green parts are the torsional bars, and the pink parts are the mechanical blocks.

D

MATLAB

The code provided performs calculations for the moment-angle graph and motion of the entire concept. It includes an optimization process to determine the optimal parameters for the moment-angle graph. The code is divided into four files. One file handles the optimization process and calls another file that calculates the moment-angle graph of the PRBM. The constraints for the optimized parameters are defined in a separate file. Finally, the last file calculates the motion of the entire concept. A detailed explanation of the underlying concepts can be found in the chapter 3.

D.1. Cost Function

```
function F = Fcost(x)
    % code about tosional springs in series with an initial prestress and .
    % linear stiffness => M=k*theta

    %% unpack x
    a1 = x(1);
    a2 = x(2);
    a3 = x(3);
    th_L_grad = x(4:end);
    %% Input
    k = [a1,a1,a2,a2,a3,a3];   % Stiffness (Nm)
    % th_L_grad is the initial torsional prestress of every spring in degrees
    th_L = th_L_grad.*pi/180;   % From degree to rad
    M = 0.001:0.005:8;          % Applied moment (Nm)

    %% Calculations moment-angle torsional bars in series
    N = length(th_L)+2; % # nodes
    m = length(M); % number of steps

    theta = zeros(m,N-2);   % angle of each node
    Ml = zeros(N-2,1);      % Moment limit corresponding to initial prestress angle

    for i =1:N-2
        Ml(i,1) = k(i)*th_L(i);     % linear moment-angle characteristic
        for j = 1:m
            if M(j)<= Ml(i)
                theta(j,i) = 0;
            else
                theta(j,i) = (M(j)-Ml(i))/k(i);
            end
        end
    end
    theta_t = sum(theta,2);         % total angle of whole system (rad)
    theta_td = theta_t.*180./pi;

    ind_120 = find(diff(sign(theta_td-121))); % find index where theta_td = 121°
    th_td = theta_td(1:ind_120);     % only take angles until 121°
    Ma = 2.*M(1:ind_120);            % prototype exists of calculated system, twice in
    parallel, so moment times two
```

```
39
40
41
42      D_th = [1,5,10,15,20,25,30,35,40,50,60,70,80,90,100,110,120];   % data for desired graph
43      D_T = [0.02,0.1,0.2,0.3,0.4,0.435,0.455,0.47,0.48,0.492,0.5,0.5,0.5,0.5,0.5,0.5,0.5];
44      lenL = length(D_th);
45      id = zeros(lenL,1);
46      Fi = zeros(lenL,1);
47      for s = 1:lenL-1
48          id(s) = find(diff(sign(th_td-D_th(s)))); % find the index closest to D_th points (x-
        coordinate of the graph)
49          Fi(s) = (interp1(th_td(id(s):id(s)+1), Ma(id(s):id(s)+1),D_th(s))-D_T(s)).^2; % least
         square error
50      end
51
52      F = abs(mean(Fi));
53  end
```

D.2. Constraints

```
1       function [c, ceq] = constraints(x)
2       [a1,a2,a3,th_L_grad] = x2u_L_0905(x);
3       c = [a1*th_L_grad(1) - (a1*th_L_grad(2)+0.01);...       % inequality constraints for Ml(i
        )< Ml(i+1)
4           a1*th_L_grad(2) - (a2*th_L_grad(3)+0.03);...        % i ranges from the first spring
        to last spring
5           a2*th_L_grad(3) - (a2*th_L_grad(4)+0.03);...
6           a2*th_L_grad(4) - (a3*th_L_grad(5)+0.03);
7           a3*th_L_grad(5) - (a3*th_L_grad(6)+0.01)];
8       ceq = [];
9   end
```

D.3. Final figure

```
1       function [Ff_th, Ff_Ma, Ff_Ml] = final_fig(x)
2       % code about tosional springs in series with an initial prestress and
3       % linear stiffness => M=k*theta
4
5       %% Input
6       a1 = x(1);
7       a2 = x(2);
8       a3 = x(3);
9       th_L_grad = x(4:end);
10
11      k = [a1,a1,a2,a2, a3,a3];   % Stiffness (Nm)
12      % th_L_grad is the initial torsional prestress of every spring in degrees
13      th_L = th_L_grad.*pi/180;   % From degree to rad
14      M = 0.001:0.005:8;          % Applied moment (Nm)
15
16      %% Calculations moment-angle torsional bars in series
17      N = length(th_L)+2; % # nodes
18      m = length(M); % number of steps
19
20      theta = zeros(m,N-2);   % angle of each node
21      Ml = zeros(N-2,1);      % Moment limit corresponding to initial prestress angle
22
23      for i =1:N-2
24          Ml(i,1) = k(i)*th_L(i);     % linear moment-angle characteristic
25          for j = 1:m
26              if M(j)<= Ml(i)
27                  theta(j,i) = 0;
28              else
29                  theta(j,i) = (M(j)-Ml(i))/k(i);
30              end
31          end
32      end
33      Ff_Ml = Ml(:);
```

```
    theta_t = sum(theta,2);         % total angle of whole system (rad)
    theta_td = theta_t.*180./pi;

    ind_120 = find(diff(sign(theta_td-120))); % find index where theta_td = 120
    Ff_th = theta_td(1:ind_120);
    Ff_Ma = 2.*M(1:ind_120).';              % calculated function
end
```

D.4. Optimization

```
OPTIONS.Algorithm = 'interior-point';
OPTIONS.MaxIterations = 100;
OPTIONS.MaxFunEvals = 10000;
OPTIONS.DiffMinChange = 0.00000001;
OPTIONS.TolX = 0.0000001;
a1_0 = [0.75]; % stiffness node 1 and 2
a2_0 = [0.3229]; % stiffness node 3 and 4
a3_0 = [0.1803]; % stiffness node 5 and 6
th_L_grad0 = [0, 10, 35, 38,100,105];   % initial torsional prestress (degrees)
x0 = [a1_0,a2_0,a3_0,th_L_grad0];
lb   = [0.17,0.17, 0.17, 0,0,0,0,0,0];
ub   = [0.7926,0.7926, 0.7926, 25,25,45,47,95,95];

A = [-1 1 0 0 0 0 0 0,0; 0, -1, 1, 0,0,0,0,0,0];  % constraints: a1 > a2 > a3
b = [0;0];
[x] = fmincon(@Fcost,x0,A,b,[],[],lb,ub,@constraints,OPTIONS);

% data for desired graph
D_th = [1; 5; 10; 15; 20; 25;30; 35; 40;50; 60;70;80;90;100;110;120];
D_T = [0.02; 0.1; 0.2; 0.3; 0.4; 0.435; 0.455; 0.47;0.48;0.492;0.5;0.5;0.5;0.5;0.5;0.5;0.5];

x_final = x;
[th_td_f, Ma_f, Ml_f] = final_fig(x_final);
figure
plot(th_td_f, Ma_f, 'LineWidth',2.5)
hold on
plot(D_th,D_T,'LineWidth',2)
legend('Graph with optimized parameters', 'Desired graph')
xlabel("Angle(°)")
ylabel("Moment(Nm)")
xlim([0 130])
```

D.5. Animation movement nodes

First part of the code, is the same code as from the cost-function.

```
%% Input
a1 = [0.5541];
a2 = [0.2515];
a3 =[0.1701];
k = [a1,a1,a2,a2,a3,a3];   % Stiffness (Nm)
% th_L_grad is the initial torsional prestress of every spring in degrees
th_L_grad=[0,10,12,14,16,18,20,22,24,26];
th_L = th_L_grad.*pi/180;   % From degree to rad
M = 0.001:0.005:8;          % Applied moment (Nm)

%% Calculations moment-angle torsional bars in series
N = length(th_L)+2; % # nodes
m = length(M); % number of steps

theta = zeros(m,N-2);   % angle of each node
Ml = zeros(N-2,1);      % Moment limit corresponding to initial prestress angle

for i =1:N-2
    Ml(i,1) = k(i)*th_L(i);     % linear moment-angle characteristic
    for j = 1:m
        if M(j)<= Ml(i)
            theta(j,i) = 0;
```

```
        else
            theta(j,i) = (M(j)-Ml(i))/k(i);
        end
     end
end
theta_t = sum(theta,2);          % total angle of whole system (rad)
theta_td = theta_t.*180./pi;

ind_120 = find(diff(sign(theta_td-121))); % find index where theta_td = 121°

%% Position of the nodes
nodes = zeros(ind_120,2,N); % Moment, x,y coordination, node number
Tnodes = zeros(2,2,N-3); % Transformation matrices
Xnodes = zeros(2,N-3); % Coordinates

for i = 1:ind_120
    for jj = 1:N-2
        Tnodes(:,:,jj) = [cos(theta(i,jj)), sin(theta(i,jj)); -sin(theta(i,jj)), cos(theta(i,
    jj))];
    end
    nodes(i,1,2) = L(1);
    nodes(i,1,3) = nodes(i,1,2) + L(2)*cos(theta(i,1));
    nodes(i,2,3) = nodes(i,2,2) + L(2)*sin(theta(i,1));

    Tcol = zeros(2,2);
    Tcol(:,:) = Tnodes(:,:,1);
    for ni = 4:N
        Xnodes = [L(ni-1)*cos(theta(i,ni-2)), L(ni-1)*sin(theta(i,ni-2))]*Tcol;
        nodes(i,1,ni) = nodes(i,1,ni-1) + Xnodes(1);
        nodes(i,2,ni) = nodes(i,2,ni-1) + Xnodes(2);
        Tnew = zeros(2,2);
        Tnew(:,:) = Tnodes(:,:,ni-2);
        Tcol = Tnew*Tcol(:,:);
    end

end

%% Plotting the movement of the nodes

figure(2)
for ii = 1:ind_120
    nnx(:,:) = nodes(ii,1,:);
    nny(:,:) = nodes(ii,2,:);
    plot(nnx(:,:),nny(:,:),'.-','MarkerSize',25,'LineWidth',2)
    xlim([min(nodes(:,1,:),[],'all'),max(nodes(:,1,:),[],'all')])
    ylim([min(nodes(:,2,:),[],'all'),max(nodes(:,2,:),[],'all')])
    xlabel('X')
    ylabel('Y')
    pause(0.01)
    axis equal
    grid on
end
```

E

Ansys

E.1. Shell simulations

For the shell concept, feasibility was assessed through simulations conducted in Ansys Workbench. Initially, a flat spring steel plate with dimensions of 400mm width and 300mm length was simulated as a shell at various thicknesses. These dimensions were estimated based on rough approximations of the body's dimensions. The stress levels obtained from the simulations are illustrated in Figure E.1. Increasing the plate's thickness increases stresses and moments, as illustrated in Figure E.2.

Subsequently, a curved profile was simulated as a shell rather than a solid structure. The chosen parameters for this simulation were a curvature of 1200mm and a thickness of 0.3mm. The results revealed that increasing the curvature and shell thickness resulted in higher stiffness, stress levels, and moments. Figure E.3 demonstrates the initial high moment followed by a decrease after buckling. This behavior could be advantageous in scenarios requiring high initial support followed by a significant drop in support beyond a certain angle. However, Figure E.4 shows that the stress levels exceed the yield stress, indicating limited feasibility for this concept unless the thickness is further reduced and curvature is increased leading to a decrease in the moment.

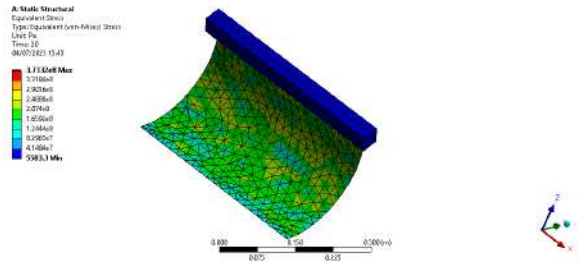

(a) Thickness of 0.3mm, average stress = 0.1021GPa.

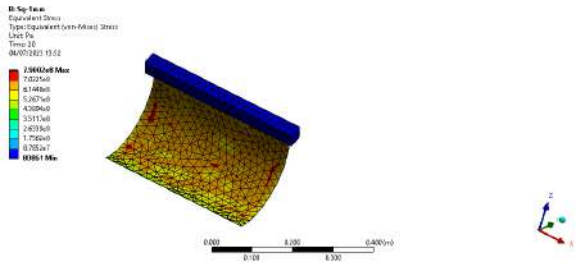

(b) Thickness of 1mm, average stress = 0.3304GPa.

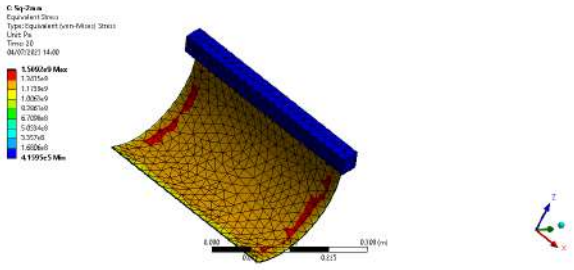

(c) Thickness of 2mm, average stress = 0.6605GPa.

Figure E.1: Stress levels of a spring steel plate with a rotation of 120°, with different thicknesses, width = 400mm, height = 300mm.

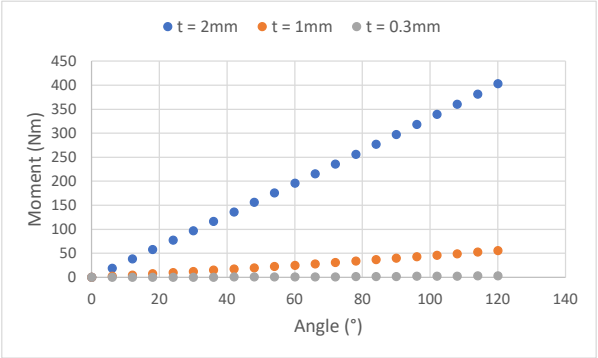

Figure E.2: Stiffness of rectangular shell for different thicknesses, width = 400mm, and length = 300mm.

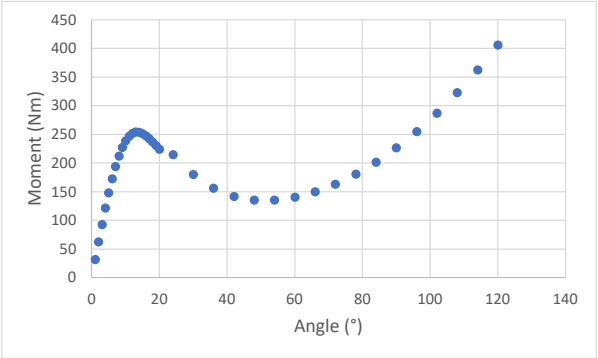

Figure E.3: Stiffness of curved shell for thickness = 0.3mm, curvature = 1200mm, width = 400mm, and length = 300mm.

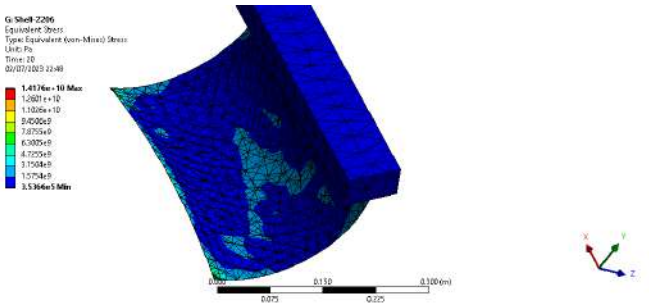

(a) Front view.

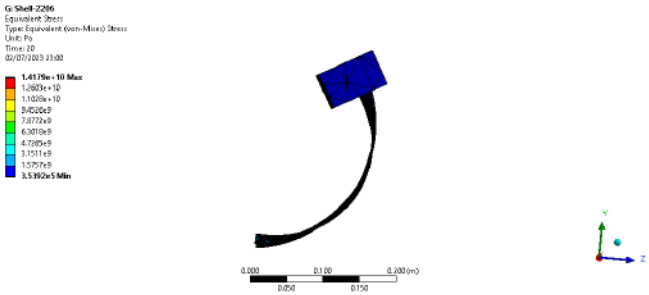

(b) Side view.

Figure E.4: Stress levels of a spring steel curved plate with a rotation of 120°, with thickness = 0.3mm, curvature = 1200mm, width = 400mm, height = 300mm. Average stress = 1.308GPa.

E.2. Torsional beams simulations

In the FEA, various cross-sections were modeled, including I-profile, U-profile, Z-profile, and X-profile. Only a section of each profile was considered, with constraints applied at the symmetry line to simulate the missing part. Initially, the FEA involved applying torque at a specific location and modeling the beams as a shell structure. A single flexure was modeled for the X-profile instead of the entire X-beam, while half of the profile was modeled for the other three profiles. Figure E.5 visually represents the modeled parts in red and the blue dot represents the location at which a torque was applied. As only a part of the entire section was modeled, symmetry constraints were added to replace the part that was not modeled. Additional constraints were applied, such as fixing one end of the beam to restrict all degrees of freedom. In contrast, the other end was constrained solely in the z-direction, perpendicular to the cross-section, as shown in Figure E.6 and Figure E.7. This constraint ensures that the beam does not experience shortening during torsion, which is undesirable for the prototype's torsional bar that has a fixed length. By multiplying the moment results by four, the moment for an X-profile was determined. The moment was multiplied by two for the other profiles to obtain the moment for the complete profile. Subsequently, a moment-angle graph was constructed to derive the stiffness.

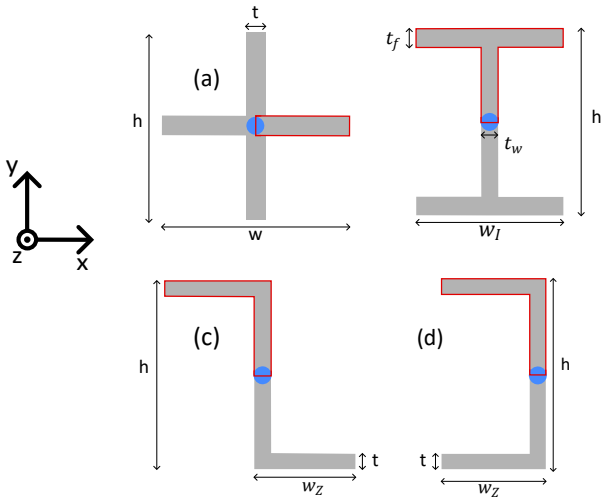

Figure E.5: Different cross sections for the FEA. Surrounded red part is the modeled part and the other part was replaced by symmetry constraint. Blue dot is where the moment is applied. (a) X-profile, (b) I-profile, (c) Z-profile, (d) U-profile.

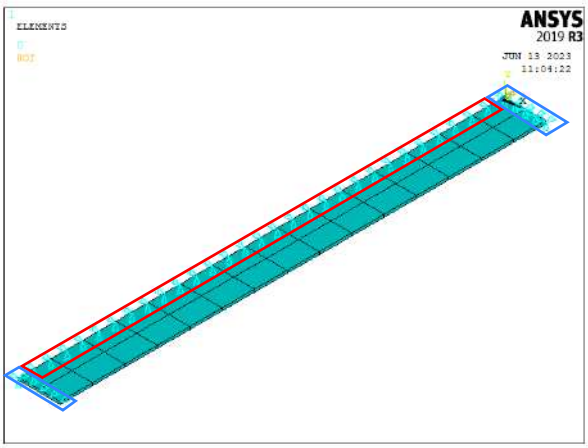

Figure E.6: Half a flexure, where the constraints enclosed by the red line are the symmetry constraints and the constraints enclosed by the blue lines are the external added constraints.

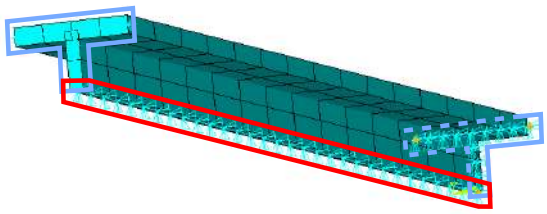

Figure E.7: I-profile and its constraints: enclosed by the red line are the symmetry constraints and the constraints enclosed by the blue lines are the external constraints.

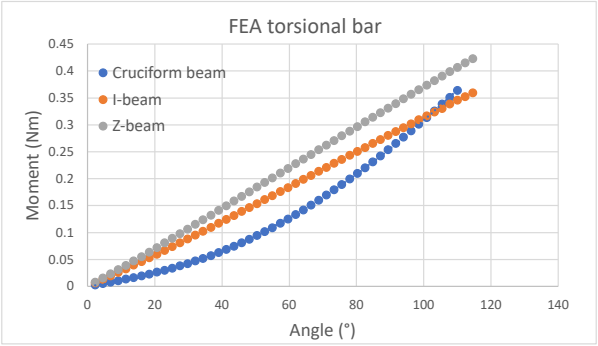

Figure E.8: FEA of I-, X-, Z-beam with the same length and volume.

The moment-angle graphs for the U-beam and Z-beam were identical since both profiles shared the same half, as shown in Figure E.8. The difference lay in their bending stiffness. The simulations were conducted using PLA material for a 15cm beam length. Additionally, all cross-sections had the same area, height, and thickness. Based on the FEA results, it was evident that the I-beam and Z-beam exhibited linear stiffness, while the cruciform beam demonstrated non-linear stiffness. The I-beam was chosen because of the prototype's requirement for linear stiffness and the goal of minimizing bending. Although the Z-beam had a higher moment than the I-beam at the same rotation angle, both the Z-beam and U-beam had lower bending stiffness than the I-beam. Therefore, the I-beam was considered the most suitable choice for the prototype.

Continuing with the I-profile, the stress levels of the I-beam were determined with the FEA so that the rotation of the deformation of the beam would stay within its elastic deformation range as can be seen in Figure E.9. Later, a FEA involved applying a uniform rotation to the cross-section of an I-beam and considering a solid instead of a shell structure. This is discussed in more detail in chapter 3, but in essence the major difference from the previous FEA is that the applied load is distributed across the entire cross-section instead of a local moment application.

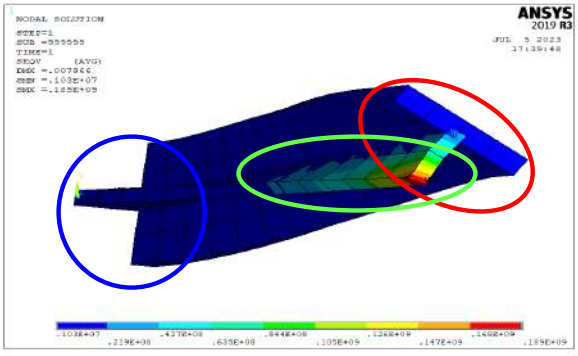

Figure E.9: Stress distribution of I-beam for a concentrated applied moment. The blue circle represents the fixed endpoint of the I-beam, the red circle represents the endpoint where the moment is applied, and the green circle represents the highest stress levels in the beam.

The FEA with a concentrated applied moment exhibits a lower stiffness compared to the experimental results, see Figure E.10. This divergence may stem from the slight deformation of the I-profile cross-section at the location where the moment is applied (indicated by the red circle in Fig. E.9), which does not occur in the prototype. Additionally, the FEA with a concentrated moment approximates the I-beam as a shell, leading to inaccurate simulations for shorter lengths. This observation is supported by Fig. E.11, where the relationship between beam length and stiffness is not inversely proportional.

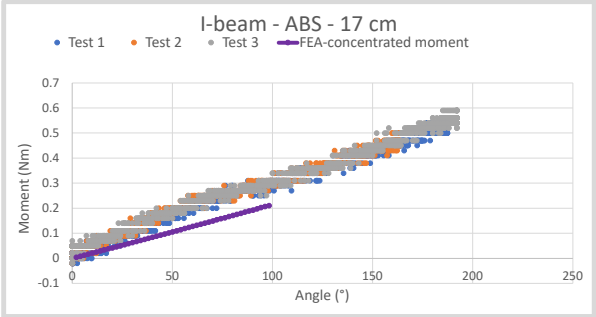

Figure E.10: Moment-angle graph of I beam in ABS, with dimensions: t_w = 0.0012m, t_f = 0.0016m, h = 0.0102m, w_I = 0.0100m, length = 0.170m.

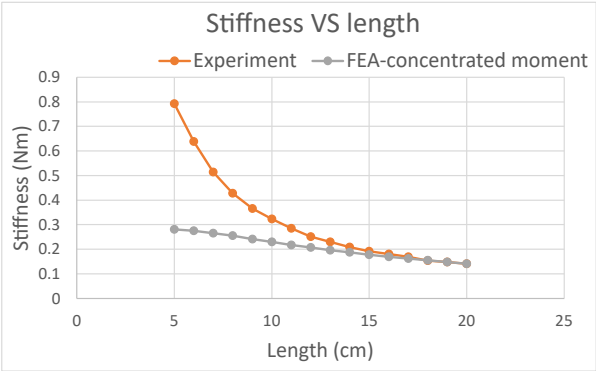

Figure E.11: Stiffness versus length of ABS I-beam.

E.3. Code

E.3.1. I-beam

```
!! general inintialization
FINISH          ! Finish previous analysis
/CLEAR,START      ! Clear data and start new analysis
/CWD,'C:\Users\Saralina\Documents\TUD\Thesis\Ansys'     ! Set the location of this file (change based on you location)
/FILNAME, APDL-I  ! Set filename in ansys

!! Set design parameters
tw  = 0.0012          !web thickness (in m)
tf  = 0.0016        !filanges thickness (in m)
bb = 0.005          !width filanges (in m)
hh = 0.0051         !height web (in m)
len = 0.1756          !length of I-beam (in m)
Middle_BC = 'Yes'       !having axissymetric boundary conditions for middle points 'Yes' or 'No'
Density  = 7850       !material properties
Poisson  = 0.29         !0.35 for PLA        0.38 for PA12      0.3 for ABS   0.29 for spring steel
Elastmod = 190e9        !3.144e9 for PLA     1.7e9 for PA12     2.65e9 for ABS  190e9 for spring steel
rotation_ang = 1.71           !applied rotation angle in rad
time_step_Rmoment = 50      !time steps to evaluate reaction moment

! yield stress    ABS 38.45e6Pa

!! Set properties
/PREP7

!element selection
ET, 1, shell281           !element type from the library can also be shell181 in some cases

mp, ex, 1, Elastmod       !Defines a linear material property as a constant or a function of temperature.
mp, nuxy, 1, Poisson
mp, dens,1, Density


!! Define key points
K,1,      0,      0,        0
K,2,      hh,     0,        0
K,3,    hh,     bb,     0
K,4,    hh,     -bb,    0
K,5,    0,      0,      len
K,6,    hh,     0,      len

!! Define lines crosssection
NUMSTR,LINE,10   ! controls the starting number for any subsequently created lines.
L,1,2
L,2,3
L,2,4

!! define Lines SHAPE
NUMSTR,LINE,100   ! controls the starting number for any subsequently created lines.
L,1,5
L,2,6

!! drag sectional lines
NUMSTR,AREA,1000   ! controls the starting number for any subsequently created area.
ADRAG,10,,,,,,100
ADRAG,11,,,,,,101
ADRAG,12,,,,,,101

! shell position regarding section mid-line
sect,1,shell,,  ! Web thickness
secdata, tw,1,0,3
secoffset,MID

```

```
!Thickness of flange
sect,2,shell,, ! Flange thickness
secdata,tf,1,0,3
secoffset,MID

!! Mesh Areas
ASEL, s, , , 1000, 1000,, 0   ! for web thickness
AATT, 1, , 1, 0, 1
AMESH,1000,1000

!! Mesh Areas
ASEL, s, , , 1001, 1000+16,, 0    ! for flanges thickness
AATT, 1, , 1, 0, 2
AMESH,1001,1000+16

!!Merges coincidents or equivalently defined items.
NUMMRG,ALL

!! Commands to visualize the elements.
/ESHAPE,1
/VIEW,1,1,1,1
eplot


!! SOLUTION
/SOLU
ANTYPE, 0   ! Static structural analysis
NLGEOM,ON   ! Set nonlinear geometry option on
EQSLV,SPARSE
autots,off
pstres,off
arclen,off
PRED,off
OUTRES,ALL,ALL


!! These are commands to assign ID's to the nodes that were meshed at the keypoints
N_M_F =   NODE(0,     0,    0)      !Node on middle fixation side section
N_M_A =   NODE(0,     0,    len)    !Node on middle actuation side section
N_M_F1 =  NODE(hh,      bb,   0)
N_M_F2 =  NODE(hh,      -bb,    0)
N_M_A1 =  NODE(hh,      bb,   len)
N_M_A2 =  NODE(hh,      -bb,    len)

!! Apply constraints to sections' middle points
D,N_M_F,,,,,,UX,UY,UZ,ROTZ
D,N_M_A,,,,,,UX,UY,
D,N_M_F1,,,,,,UZ,ROTZ
D,N_M_A1,,,,,,UZ
D,N_M_F2,,,,,,UZ,ROTZ
D,N_M_A2,,,,,,UZ

!! putting B.C in the centerline for axisymmetric condition
*IF, Middle_BC,EQ,'Yes',THEN
  *DO,N_Node, 1, 100, 1

    D,NODE(0,   0,    N_Node*len/100),,,,,,UX,UY,

  *ENDDO
*ENDIF

! put boundary condition from node 1 to 2
*DO,N_Node, 1, 100, 1

    D,NODE(N_Node*hh/100,   0,    0),,,,,,UX,UY,UZ

*ENDDO

! put boundary condition from node 2 to 3
*DO,N_Node, 2, 100, 1

```

```
    D,NODE(hh,    N_Node*bb/100,    0),,,,,,UX,UY,UZ

*ENDDO
! put boundary condition from node 2 to 4
*DO,N_Node, 2, 100, 1

    D,NODE(hh,    -N_Node*bb/100,   0),,,,,,UX,UY,UZ

*ENDDO

! put boundary condition from node 5 to 6
*DO,N_Node, 1, 100, 1

    D,NODE(N_Node*hh/100,   0,    len),,,,,,UZ

*ENDDO
! put boundary condition from node 6 to endpoint filanges
*DO,N_Node, 1, 100, 1

    D,NODE(hh,    N_Node*bb/100,    len),,,,,,UZ

*ENDDO
*DO,N_Node, 1, 100, 1

    D,NODE(hh,    -N_Node*bb/100,   len),,,,,,UZ

*ENDDO


!! Apply rotation and measuring the reaction moment
/SOLU
OUTRES,,ALL                     ! After this command, loadstep data is saved for every
    substep
KBC,0                       ! ramped loading
DELTIM, 1/time_step_Rmoment, 1E-3, 1, ON    ! Command to specify the number of steps in the
    analysis (this can be necessary for nonlinear systems where too big steps cause crashes)
D,N_M_A,ROTZ,rotation_ang
solve


!! Commands to plot output and save results
*GET, N_steps, active, 0, solu, ncmss     ! Count the number of substeps to size the table
    correctly
/POST26                     ! Go to postprocessor menu
NSOL,2,N_M_A,ROT,Z,Rotation                   ! Get the angle data of the node N_M_A
RFORCE,3,N_M_A,M,Z,RMoment                ! Get the reaction moment of the node N_M_A
/AXLAB, X, Angle in rad
/AXLAB, Y, Reaction moment in N.m
XVAR,2                      ! Put the angle on the X axis in the plot
PLVAR,3                     ! Plot the reaction moment on the Y axis


!! The commands below are to save the plot in a .txt file
*CREATE,scratch,gui
    *DEL,VAR_export
    *DIM,VAR_export,TABLE,N_steps,3     ! Set size of the table for results export
     VGET,VAR_export(1,0),1
     VGET,VAR_export(1,1),2
     VGET,VAR_export(1,2),3
    /OUTPUT,'RESULTS_I_Beam','txt','C:\Users\Saralina\Documents\TUD\Thesis\Ansys' ! In this
    line you specify the location to export results
   *VWRITE,VAR_export(1,0),VAR_export(1,1),VAR_export(1,2)
       %G, %G, %G
    /OUTPUT,TERM
    *END
   /INPUT,scratch,gui
```

E.3.2. U- and Z-beam

```
! moment-angle Z-profile
```

```
2
3  !! general inintialization
4  FINISH          ! Finish previous analysis
5  /CLEAR,START      ! Clear data and start new analysis
6  /CWD,'C:\Users\Saralina\Documents\TUD\Thesis\Ansys'     ! Set the location of this file (
       change based on you location)
7  /FILNAME, APDL-Z  ! Set filename in ansys
8
9  !! Set design parameters
10 t   = 0.0008          !web thickness (in m)
11 wz = 0.0134         !width filanges (in m)
12 hh = 0.013          !half of total height (in m)
13 len = 0.150         !length of I-beam (in m)
14 Middle_BC = 'Yes'       !having axissymetric boundary conditions for middle points 'Yes' or
       'No'
15 Density  = 1010       !material properties
16 Poisson  = 0.3          !0.35 for PLA        0.38 for PA12      0.29 for spring steel
17 Elastmod = 2.65e9       !3.144e9 for PLA     1.7e9 for PA12     190e9 for spring steel
18 rotation_ang = 2            !applied rotation angle in rad
19 time_step_Rmoment = 50      !time steps to evaluate reaction moment
20
21
22 !! Set properties
23 /PREP7
24
25 !element selection
26 ET, 1, shell281            !element type from the library can also be shell181 in some cases
27
28 mp, ex, 1, Elastmod        !Defines a linear material property as a constant or a function of
       temperature.
29 mp, nuxy, 1, Poisson
30 mp, dens,1, Density
31
32
33 !! Define key points
34 K,1,      0,      0,        0
35 K,2,      b,      0,        0
36 K,3,    b,      -hh,    0
37 K,4,    b,      0,      len
38
39
40 !! Define lines crosssection
41 NUMSTR,LINE,10   ! controls the starting number for any subsequently created lines.
42 L,1,2
43 L,2,3
44
45 !! define Lines SHAPE
46 NUMSTR,LINE,100   ! controls the starting number for any subsequently created lines.
47 L,2,4
48
49
50 !! drag sectional lines
51 NUMSTR,AREA,1000   ! controls the starting number for any subsequently created area.
52 ADRAG,10,,,,,,100
53 ADRAG,11,,,,,,100
54
55
56 ! shell position regarding section mid-line
57 sect,1,shell,,  ! Web thickness
58 secdata, t,1,0,3
59 secoffset,MID
60
61
62 !! Mesh Areas
63 ASEL, s, , , 1000, 1000+16,, 0  ! for web thickness
64 AATT, 1, , 1, 0, 1
65 AMESH,1000,1000+16
66
67
68
69 !!Merges coincidents or equivalently defined items.
```

```
NUMMRG,ALL

!! Commands to visualize the elements.
/ESHAPE,1
/VIEW,1,1,1,1
eplot


!! SOLUTION
/SOLU
ANTYPE, 0   ! Static structural analysis
NLGEOM,ON   ! Set nonlinear geometry option on
EQSLV,SPARSE
autots,off
pstres,off
arclen,off
PRED,off
OUTRES,ALL,ALL


!! These are commands to assign ID's to the nodes that were meshed at the keypoints
N_M_F =   NODE(0,     0,    0)      !Node on middle fixation side section
N_M_A =   NODE(0,     0,    len)    !Node on middle actuation side section
N_M_F1 =  NODE(wz,      0,    0)
N_M_F2 =  NODE(wz,      -hh,    0)


!! Apply constraints to sections' middle points
D,N_M_F,,,,,,UX,UY,UZ,ROTZ
D,N_M_A,,,,,,UX,UY,
D,N_M_F1,,,,,,UZ,ROTZ
D,N_M_F2,,,,,,UZ,ROTZ


!! putting B.C in the centerline for axisymmetric condition
*IF, Middle_BC,EQ,'Yes',THEN
  *DO,N_Node, 1, 100, 1

    D,NODE(0,   0,    N_Node*len/100),,,,,,UX,UY,

  *ENDDO
*ENDIF

! put boundary condition from node 1 to 2
*DO,N_Node, 1, 100, 1

    D,NODE(N_Node*wz/100,   0,    0),,,,,,UX,UY,UZ

*ENDDO

! put boundary condition from node 2 to 3
*DO,N_Node, 2, 100, 1

    D,NODE(wz,    -N_Node*hh/100,   0),,,,,,UX,UY,UZ

*ENDDO

! put boundary condition from node 4 to 2
*DO,N_Node, 1, 100, 1

    D,NODE(N_Node*wz/100,   0,    len),,,,,,UZ

*ENDDO
! put boundary condition from node 4 to endpoint filanges
*DO,N_Node, 1, 100, 1

    D,NODE(wz,    -N_Node*hh/100,   len),,,,,,UZ

*ENDDO


```

```
!! Apply rotation and measuring the reaction moment
/SOLU
OUTRES,,ALL                     ! After this command, loadstep data is saved for every substep
KBC,0                         ! ramped loading
DELTIM, 1/time_step_Rmoment, 1E-3, 1, ON    ! Command to specify the number of steps in the analysis (this can be necessary for nonlinear systems where too big steps cause crashes)
D,N_M_A,ROTZ,rotation_ang
solve


!! Commands to plot output and save results
*GET, N_steps, active, 0, solu, ncmss     ! Count the number of substeps to size the table correctly
/POST26                       ! Go to postprocessor menu
NSOL,2,N_M_A,ROT,Z,Rotation                   ! Get the angle data of the node N_M_A
RFORCE,3,N_M_A,M,Z,RMoment                ! Get the reaction moment of the node N_M_A
/AXLAB, X, Angle in rad
/AXLAB, Y, Reaction moment in N.m
XVAR,2                        ! Put the angle on the X axis in the plot
PLVAR,3                       ! Plot the reaction moment on the Y axis


!! The commands below are to save the plot in a .txt file
*CREATE,scratch,gui
    *DEL,VAR_export
    *DIM,VAR_export,TABLE,N_steps,3     ! Set size of the table for results export
     VGET,VAR_export(1,0),1
     VGET,VAR_export(1,1),2
     VGET,VAR_export(1,2),3
    /OUTPUT,'RESULTS_Z_Beam','txt','C:\Users\Saralina\Documents\TUD\Thesis\Ansys' ! In this line you specify the location to export results
   *VWRITE,VAR_export(1,0),VAR_export(1,1),VAR_export(1,2)
       %G, %G, %G
    /OUTPUT,TERM
    *END
   /INPUT,scratch,gui
```

F

Material certificate for spring steel

MATERIAALCERTIFICAAT: EN 10204/3.1

Deka B.V. 9

Uw referentie: mail

Smeltnummer:	Batch nr	Onze referentie:	Test rapport nr	Bron nr
922610	MIO-14-0706/5B	VO-16-1644	00001883	443

MATERIAALOMSCHRIJVING

Roestvast staal Austenitisch 1.4310 C1300 - Hard gewalst
EN 10151 EN ISO 9445-1

MECHANISCHE EIGENSCHAPPEN + AFMETINGEN

Dikte/Dia (mm)	Breedte (mm)	Lengte (mm)	Aantal
2,5	310	2000	124

Rekgrens (Rp 0,2 %: N/mm² - MPa)	Treksterkte (N/mm²)	Korrelgrootte
1120	1390	

Rek (%)	Hardheid	Ruwheid
21,25 %		

CHEMISCHE EIGENSCHAPPEN (%)

Ag	Al	As	B	Be	Bi	C	Ca	Cd	Ce
	0,002		0,0006			0,106			
Co	Cr	Cu	Fe	H	Li	Mg	Mn	Mo	N
0,169	16,76	0,34					1,21	0,32	0,06
Na	Nb/Cb	Ni	O	P	Pb	Pd	S	Sb	Se
	0,008	6,51		0,03			0,001		
Si	Sn	Ta	Te	Ti	V	W	Y	Zn	Zr
0,85				0,001					

Andere: ceq: 4,1998

05/05/17

Deze gegevens werden integraal overgenomen van het originele certificaat van de walserij.
Dit document werd door een computer opgesteld en is zonder handtekening geldig.

Figure F.1: Material certificate for spring steel strip in Dutch. Red square represents the yield strength.